Petrogenesis of Late Triassic adakitic rocks and basalts from the southern Lhasa: Insights into subduction initiation of Neo-Tethys

Cheng Li[a, b], Lin Ma[a, b]*, Andrew C. Kerr[c], Wei Dan[a, b], Qiang Wang[a, b] , Zhiwei Yu[a, b], Wei Qiao[a, b], Rui Pu[a, b], Fan Yang[a, b]

[a] *State Key Laboratory of Deep Earth Processes and Resources (DEEPER), Guangzhou Institute of Geochemistry, Chinese Academy of Sciences, Guangzhou 510640, China*

[b] *College of Earth and Planetary Sciences, University of Chinese Academy of Sciences, Beijing 100049, China*

[c] *School of Earth and Environmental Sciences, Cardiff University, Cardiff, Wales CF10 3AT, UK*

Corresponding author. E-mail: Lin Ma (malin@gig.ac.cn)

Abstract

Although a critical part of reconstructing the dynamic evolution of the Neo-Tethyan ocean, the timing and mechanism of subduction initiation remains highly controversial. In this contribution, we report petrological and geochemical data for newly identified Late Triassic Aza biotite granodiorites and Chango basalts in southern Tibet. The Aza biotite granodiorites (ca. 236 Ma) display adakitic affinities. These granodiorites are characterized by high SiO_2 (62.8–68.6 wt.%), moderate MgO (1.3–3.1 wt.%), high Sr (444–546 ppm) and low Y (8.4–14.0 ppm) and Yb (0.87–1.48 ppm) contents, along with high Na_2O/K_2O (0.9–2.1), Sr/Y (35.3–59.0) and La/Yb (7.4–24.4) ratios and positive $\varepsilon_{Nd}(t)$ values of +6.1 to +6.7, similar to melts of subducting oceanic slab. The Chango basalts (ca. 219 Ma) have typical arc basalt features, such as enriched large ion lithophile elements (LILE) and depleted high field strength elements (HFSE) with $\varepsilon_{Nd}(t)$ of +6.4 to +7.2, suggesting derivation from a metasomatized asthenospheric mantle wedge source. The presence of these two suites of magmatic rocks provides solid evidence for the early subduction of the Neo-Tethys Ocean during the Late Triassic. Moreover, numerical modelling indicates that the closure of the Sumdo Ocean (ca. 240 Ma) is the most likely potential candidate as the driving force for the subduction initiation of the Neo-Tethys Ocean. The closure of the Sumdo Ocean and the earliest magmatic rocks related to subduction in southern Lhasa jointly constrain the onset of Neo-Tethys subduction to around 240 Ma.

Keywords: Subduction initiation timing, Subduction initiation mechanism,

Geodynamics of plate convergence, Neo-Tethys, Southern Tibet

1 Introduction

The Tethys tectonic domain records the long-term evolution of Tethys oceans (Zhu et al., 2022) extending from northeastern Australia into the Alpine-Mediterranean mountain chains, via Tibetan and Iran Plateaus. This makes it a geologically complex region and one of the richest areas for mineral deposits and petroleum resources in the world (Zhu et al., 2022). The Tethys Ocean was located between the Gondwana and Laurasia supercontinents during the Phanerozoic, and its development was associated with the rifting and accretion of Gondwana-derived terranes to the Eurasia supercontinent (Wan et al., 2019). As one of the main branches of the Tethyan oceans, the Neo-Tethys opened during the Late Paleozoic due to the separation of the Lhasa block from Gondwana and finally closed during the Cenozoic, leading to the formation of the immense Tibetan Plateau (Dan et al., 2021; Zhu et al., 2023). However, the early tectonic evolutionary history of the Neo-Tethys Ocean, particularly the timing of its subduction initiation, remains unclear, and this hinders reconstruction of the tectonic evolution of this disappeared ocean.

Initially, it was thought that the subduction initiation of the Neo-Tethys Ocean occurred in the Early Cretaceous, mainly based on the dating results of the Yarlung-Zangbo ophiolite and the arc-like magmatism in southern Lhasa (e.g., Dai et al., 2013; Wen et al., 2008). However, our understanding of the timing of subduction initiation has changed with the subsequent discovery of many more Jurassic-to-Middle Triassic

arc-like magmatic rocks in southern Lhasa (e.g., Kang et al., 2014; Wang et al., 2016, 2022b; Zhu et al., 2023). Some have alternatively suggested that these Triassic-Jurassic arc-like magmatic rocks in southern Lhasa might be the result of the southward subduction of the Bangong–Nujiang Tethys slab (e.g., Huang et al., 2021; Zhu et al., 2011, 2013). In addition, the most reliable petrological evidence for determining the onset of subduction, such as boninite and forearc basalt, are no longer present due to significant subduction erosion (Huang et al., 2022) and potential re-initiation of subduction during the Early Cretaceous (Xiong et al., 2016). Therefore, although crucial for understanding and reconstructing the evolution of the Neo-Tethys Ocean the timing and mechanism of subduction initiation in the Tibetan Plateau region remains a highly debated issue. It is worth noting that uncertainties in determining the timing of subduction initiation are not unique to the Tibetan region and are common issue for the reconstruction of ancient convergent orogens worldwide.

In this contribution, we present petrological, geochronological, and geochemical data for newly identified biotite granodiorites and basalts in southern Tibet. Our results indicate that these Late Triassic biotite granodiorites and basalts were derived from subducted oceanic slab and metasomatized depleted mantle, respectively, which provides clear evidence for the subduction of the Neo-Tethys Ocean during the Late Triassic.

2 Geological background and samples

2.1 Geological background

The Tethys evolved from a Paleozoic-Mesozoic ocean into three long-term evolving oceans: Proto-Tethys, Paleo-Tethys, and Neo-Tethys, and their life cycles span the entire Phanerozoic era (Wan et al., 2019). As an important part of the Tethys domain, the Tibetan Plateau preserves a complete record of this multi-stage Tethys evolution. Within the Tibetan Plateau, a series of east-west Tethyan closure sutures are preserved. From north to south, they are the Aemye Ma-chhen-Kunlun-Muzitag, Jinsha and Longmu Co-Shuanghu sutures formed by the closure of the Paleo-Tethys Ocean, and the Bangong–Nujiang, Sumdo and Yarlung–Zangbo sutures formed by the closure of the Neo-Tethys Ocean (Fig. 1a) (e.g., Hao et al., 2025; Liu et al., 2020; Yin and Harrison, 2000; Zhu et al., 2013). These sutures demarcate several Gondwana-derived blocks including the Songpan–Ganze, Qiangtang, Lhasa, and Himalaya blocks which have developed since the Early Paleozoic during the evolution of various Tethyan Oceans (Fig. 1a).

The Indus-Yarlung Zangbo suture zone (IYZSZ) is one of the most important tectonic boundaries in the Tibetan Plateau. It marks the site where the Indus-Yarlung Zangbo Tethyan Ocean lithosphere was consumed at a subduction zone dipping northward beneath the Lhasa block (Yin and Harrison, 2000; Zhu et al., 2013). The igneous age of the diabases or gabbros from the ophiolite sequences along the IYZSZ has been estimated at 163–120 Ma (Dai et al., 2013; Zhu et al., 2013). In recent years, a number of Early Permian-Middle Triassic ophiolites have also been identified within the IYZSZ (Liu et al., 2020) and these suggest that the opening of the Neo-Tethys Ocean can be traced to as early as Early Permian (Liu et al., 2020).

As the upper plate of the Neo-Tethys subduction zone, the Lhasa block can be further subdivided into the northern, central, and southern Lhasa subblocks, separated by the Shiquanhe-Namco ophiolite mélange zone and the Luobadui–Milashan Fault, respectively (Fig. 1b) (Zhu et al., 2011). Based on zircon in situ U–Pb and Lu–Hf isotopic and bulk-rock geochemical data of Mesozoic–Early Tertiary magmatic rocks, the Lhasa block contains ancient basement rocks of Proterozoic and Archean ages (up to 2870 Ma) in central Lhasa and in the eastern part of southern Lhasa. Younger and more juvenile Phanerozoic crust was accreted toward both the northern and southern edges of the block (Ma et al., 2019; Zhu et al., 2011, 2013). The southern Lhasa subblock thus is likely to have been a microcontinent that underwent extensive Phanerozoic crustal reworking and growth (Ma et al., 2019).

Southern Lhasa is the southernmost part of the Asian continent before India–Asia collision and the leading edge of the Neo-Tethys subduction zone. The sedimentary cover in the southern Lhasa subblock is largely restricted to the eastern portion (Zhu et al., 2013). The Paleozoic Nyingchi Group (Dong et al., 2010) and the Middle–Late Triassic (ca. 237-212 Ma) Changguo Formation littoral-shallow marine sedimentary rocks (e.g., marble, conglomerate, siltstone) potentially represent the oldest cover unit of this subblock (Huang et al., 2021; Wang et al., 2022a).

The Phanerozoic magmatic and metamorphic rocks record geodynamic evolution information of Lhasa, which is crucial for understanding the development of Tethys. Scarce Cambrian (~496 Ma) orthogneiss intrusive rocks with limited geochemical data have been reported from southern Lhasa (Dong et al., 2010). Late

Devonian–Early Carboniferous Zhengga amphibolite and two-mica gneissic granite (366–353 Ma, Ma et al., 2019) also occur in the southern Lhasa subblock. The Zhengga amphibolite has low SiO_2 and high MgO, Cr, and Ni contents with positive $\varepsilon_{Nd}(t)$ of +3.3 to +8.0 and zircon $\varepsilon_{Hf}(t)$ of +0.9 to +11.2, and low zircon $\delta^{18}O$ of 5.7±0.2‰, which are proposed to have formed by decompression melting of asthenosphere during intracontinental back-arc extension (Ma et al., 2019). A Permo-Carboniferous (353-264 Ma) magmatic gap occurs in southern Lhasa (Ma et al., 2022), coeval with the Pikang granites (~263 Ma, Zhu et al., 2009) and high-pressure Sumdo eclogite (~262 Ma, Yang et al., 2009) in central Lhasa. The Pikang peraluminous granite magmatism and Sumdo high-pressure metamorphism are coeval with the regional angular unconformity between the Middle and the Upper Permian, all of which have been linked to an orogeny referred to as the Permian Orogeny (Zhu et al., 2009). Middle Triassic–Early Jurassic magmatic rocks have been found in the central and southern Lhasa subblocks. Middle Triassic-Early Jurassic intrusive rocks in central Lhasa are silicic, metaluminous to peraluminous with negative $\varepsilon_{Hf}(t)$ values (−17.3 to −2.5), suggesting anatexis of ancient continental crust (Yu, 2020; Zhu et al., 2011, 2013). While in southern Lhasa, the Middle Triassic–Early Jurassic volcanic rocks exhibiting arc-like characteristics with depleted Sr-Nd-Hf isotope compositions are derived by partial melting of a heterogeneous mantle source (e.g., Wang et al., 2016; Zhu et al., 2008).

2.2 Samples collected for this study

The samples in this study were collected close to the towns of Aza and Chango, located approximately 30-40 km southeast of Lhasa City (Figs. 1c, 2a-b; Table S1). The Aza biotite granodiorite intrudes into the lower section of the Middle-Late Triassic (ca. 237-212 Ma) Changguo Formation that is a newly established stratigraphic unit (Wang et al., 2016, 2022a; Huang et al., 2021), while the Chango basalt is a shallow constituent unit of this volcanic-sedimentary sequence. The Aza biotite granodiorite samples display a massive structure with granular texture and generally consist (vol.%) of plagioclase (40-45%), quartz (20-25%), biotite (10-15%), amphibole (5-10%), and opaque minerals (5-10%) (Figs. 2c-d). The plagioclase, quartz, biotite and amphibole crystals in the Aza biotite granodiorites are mainly subhedral (Figs. 2c-d). The Chango basalt samples have massive structure with porphyritic textures. The phenocryst assemblage is dominated by plagioclase (10-15%) and clinopyroxene (15-20%) (Figs. 2e-f). Subhedral-anhedral plagioclase crystals show albitization (Figs. 2e-f; Table S2), characterized by cellular and locally turbid textures. The subhedral-anhedral clinopyroxene crystals are commonly observed to be partially or completely replaced by actinolite, indicating that these rocks undergone varying degrees actinolitization. (Figs. 2e-f; Table S2). The groundmass dominantly consists of crypto-crystalline or glassy, and locally visible fine-grained plagioclase and clinopyroxene.

3 Results

Analytical methods are given in Text S1 in the supporting information. Mineral composition, zircon U-Pb geochronology, major and trace elements, Sr-Nd isotope, and

zircon O isotope data for the samples are given in Tables S2–S6, respectively.

3.1 Mineral compositions

Representative mineral compositions from the samples are listed in Table S2.

Plagioclase in the Aza biotite granodiorites mainly consists of albite ($Ab_{91-96}An_{4-9}Or_{0-1}$) and oligoclase ($Ab_{76-89}An_{11-23}Or_{0-2}$). Plagioclase in the Chango basalts is predominantly labradorite ($Ab_{31-44}An_{56-69}Or_{0}$) and bytownite ($Ab_{23-27}An_{73-76}Or_{0}$), with a small amount of albite ($Ab_{91-99}An_{1-9}Or_{0-1}$).

Based on the amphibole classification of Leake et al. (1997), all of the amphiboles from this study belong to the calcic group ($Ca_B > 1.5$), which exhibit $(Na + K)_A < 0.5$, $Ca_A < 0.5$, and all display high Si content (Si in formula > 6.5). The amphiboles in the Aza biotite granodiorites are mainly composed of magnesiohornblende, whereas those in the Chango basalts have characteristics of actinolite and magnesiohornblende.

3.2 Zircon U-Pb ages

One biotite granodiorite sample (21AZ05-1) and one basalt sample (21CG04-1) were selected for zircon dating. Zircon U-Pb isotopic data are given in Tables S3-S4.

Zircons from the biotite granodiorite have crystal lengths of ~50–200 μm, length/width ratios from 1:1 to 3:1 and display oscillatory zoning of magmatic growth (Fig. 3a). The zircon crystals from biotite granodiorite (21AZ05-1) show variable U (247–798 ppm) and Th (82–831 ppm) contents with Th/U ratios ranging from 0.33 to

1.07, indicating a magmatic origin (Hoskin and Black, 2000). Twenty-five analyses of zircons from sample 21AZ05-1 yield a weighted mean $^{206}Pb/^{238}U$ age of 235.8±2.5 Ma (LA-ICP-MS; MSWD=0.8; Fig. 3a).

According to the internal morphology shown in CL images (Fig. 3b), zircons from the basalt can be divided into two categories: magmatic and inherited zircons. The magmatic zircons have crystal lengths of ~50–100 μm, length/width ratios from 1:1 to 2:1 and display oscillatory zoning of magmatic growth. The inherited zircon grains display round shapes, with average crystal lengths being 40–60 μm and length-to-width ratios of 1:1. The magmatic and inherited zircons have variable Th (85-485 ppm and 42-1470 ppm, respectively) and U (286-1085 ppm and 58-1325 ppm, respectively) contents, with Th/U ratios of 0.30-1.09 and 0.33-1.11, respectively, indicating a magmatic origin for both. Four analyzed spots on inherited zircons gave old ages ranging from Paleoproterozoic to Early Permian (1951.6–293.1Ma) (Fig. 3b). The six magmatic zircons gave concordant $^{206}Pb/^{238}U$ ages of 223.4 to 213.2 Ma, with a weighted mean age of 219.2 ± 2.9 Ma (SIMS; MSWD = 1.09) (Fig. 3b).

3.3 Major and trace element data

Major and trace element compositions are given in Table S5.

The Aza biotite granodiorites have high SiO_2 (62.8–68.6 wt.%), MgO (1.3–3.1 wt.%), Na_2O (3.8-5.1 wt.%) contents and Na_2O/K_2O (0.9-2.1) values. On the SiO_2 vs. Nb/Y diagram, the samples plot in the rhyodacite or dacite fields (Fig. 4a). They are characterized by high $Mg^{\#}$ (46-58) values and low Cr (4-44 ppm) and Ni (3-26 ppm)

contents. The Aza samples have calc-alkaline and metaluminous characteristics (A/CNK = molecular $Al_2O_3/(CaO + Na_2O + K_2O)$ = 0.91-0.99; Figs. 4b-c). They have chondrite-normalized rare earth element (REE) patterns with negligible Eu anomalies (δEu = 0.92-1.03; Fig. 5a) and are enriched in light rare earth elements (LREEs) relative to heavy rare earth elements (HREEs) with $(La/Yb)_N$ of 5.3-17.5. The Aza samples are also characterized by enrichment in LILEs and depletion of HFSEs, with negative Nb-Ta-Ti anomalies and positive Sr anomalies (Fig. 5b). It is worth noting that the biotite granodiorite samples show affinity of adakite with low Yb and Y (Yb = 0.87-1.48 ppm; Y = 8.9-14.0 ppm) and high Sr (444-546 ppm) contents and high Sr/Y (35.3-59.0) and La/Yb (7.4-24.4) ratios (Defant and Drummond, 1990; Martin, 1999) (Fig. 4d).

The Chango basalts have variable SiO_2 (42.9-52.3 wt.%), MgO (4.8-8.6 wt.%), Cr (14-349 ppm), Ni (22-92 ppm) contents and $Mg^{\#}$ (51-72) values. On a SiO_2 vs. Nb/Y diagram, the samples plot in the basalt field (Fig. 4a) and exhibit calc-alkaline geochemical characteristics (Fig. 4b). The Chango basalts are characterized by enriched chondrite-normalised LREE ($(La/Yb)_N$ = 2.11-6.03) and relatively flat HREE ($(Dy/Yb)_N$ = 1.21-1.48) patterns without marked Eu anomalies (Eu/Eu* = 0.83-1.04) (Fig. 5c). They are also characterized by the enrichment of LILEs and depletion of HFSEs, with negative Nb, Ta, Ti concentration anomalies on primitive mantle-normalised plots (Fig. 5d).

3.4 Sr–Nd–O isotopic data

The whole-rock Sr-Nd and zircon O isotopic compositions of representative

samples are listed in Tables S5-S6. The initial Sr-Nd isotopic ratios are calculated based on their crystallization ages. As shown in the plot of $\varepsilon_{Nd}(t)$ vs. $(^{87}Sr/^{86}Sr)_i$ (Fig. 6), the biotite granodiorites have low initial $^{87}Sr/^{86}Sr$ ratios (0.7027-0.7035) and positive $\varepsilon_{Nd}(t)$ values (+6.1 to +6.7). The basalts have initial $^{87}Sr/^{86}Sr$ ratios from 0.7034 to 0.7048 and positive $\varepsilon_{Nd}(t)$ values (+6.4 to +7.2).

Two Aza biotite granodiorite samples (21AZ05-1 and 24AZ03-7) have similar zircon $\delta^{18}O$ values (5.36 to 6.04 ‰ and 5.55 to 6.40 ‰), which are comparable to or slightly higher than those (5.3 ± 0.3‰) of igneous zircons in equilibrium with mantle magmas (Valley, 2003).

4 Discussion

4.1 Petrogenesis

4.1.1 Effects of alteration and crustal assimilation

Alteration and crustal assimilation generally have impacts on the composition of magmatic rocks. Therefore, it is necessary to first assess the influence of these processes, before discussing the origin and evolution process of magmatic rocks using the bulk rock composition.

For the Aza biotite granodiorites, low LOI (0.56-1.78 wt.%) values and lack of altered minerals (Figs. 2c-d) suggest insignificant impact of metamorphism or sub-solidus alteration. On the other hand, based on the presence of albite and actinolite and variable LOI (0.5-7.2 wt.%), the Chango basalts may have undergone low-grade metamorphism or variable degrees of alteration after emplacement. Generally, Zr is

considered immobile during low- to medium-grade alteration (Pearce et al., 1992; Wood et al., 1979). Hence, correlation of elements with Zr can be used to assess the mobility of elements (Polat et al., 2002). For the Chango basalts, HFSEs (e.g., Nb, Ta, Th, and Hf) and REEs show a good correlation with Zr, while LILEs (e.g., Rb, Ba, Sr and K) exhibit a scattered distribution (Fig. 7). The following discussion on the origin of the Chango basalts thus will focus on the HFSEs and REEs rather than LILEs.

Crustal contamination is almost inevitable for mantle-derived melts during their ascent through continental crust or their evolution within a crustal magma chamber (e.g., Castillo et al., 1999). For the Aza biotite granodiorites, relatively uniform $\varepsilon_{Nd}(t)$ (+6.1 to +6.7) values and decreasing $(^{87}Sr/^{86}Sr)_i$ with increasing SiO_2 are inconsistent with expected trends of continental crustal contamination (Figs. 8a-b). For the Chango basalts, relatively uniform and positive $\varepsilon_{Nd}(t)$ (+6.4 to +7.2) values, as well as a lack of correlation between $\varepsilon_{Nd}(t)$ values and $^{147}Sm/^{144}Nd$ (Fig. 8c), also indicate insignificant crustal contamination (Vervoort and Blichert-Toft, 1999). Moreover, the constancy of $\varepsilon_{Nd}(t)$ values with changes in MgO contents further supports the above inference (Fig. 8d).

4.1.2 Origin of Aza biotite granodiorites

The high Sr, low Y and Yb contents of Aza biotite granodiorites with high Sr/Y and La/Yb ratios show affinities to adakites (Fig. 4d). Adakitic rocks can be generated by a variety of mechanisms, such as melting of subducted young and hot oceanic crust (Defant and Drummond, 1990), partial melting of thickened basaltic lower crust (e.g.,

Liu et al., 2010), crustal assimilation and low-pressure fractional crystallization from parental basaltic magmas (Castillo et al., 1999), and high-pressure crystallization (involving garnet) of mafic magmas derived from mantle wedge peridotites (Macpherson et al., 2006). We evaluate these alternative processes in the following sections with specific reference to the Aza adakitic rocks.

Depleted Nd isotope compositions ($\varepsilon_{Nd}(t)$ = +6.1 to +6.7) of the Aza biotite granodiorites, similar to those of the Yarlung Tsangpo ophiolites ($\varepsilon_{Nd}(t)$ = +3.3 to +9.8) (e.g., Zhang et al., 2005, 2020) and oceanic slab-derived adakites ($\varepsilon_{Nd}(t)$ = +3.6 to +6.4) (e.g., Tian et al., 2022; Wang et al., 2019, 2022c) (Fig. 6), suggest a potential source of depleted mantle, oceanic crust or juvenile continental crust. In addition, for adakitic magmas derived from the low-pressure (involving amphibole) or high-pressure (involving garnet) fractional crystallization of mantle-derived magma, a marked depletion of middle or heavy REE is expected, given the enrichment of MREE and HREE in amphiboles and garnets respectively (Castillo et al., 1999; Macpherson et al., 2006). However, the Aza biotite granodiorites show uniform $(Dy/Yb)_N$ (0.9-1.2) (Fig. S1) and flat HREE patterns with negligible Eu anomalies, which indicate minimal fractional crystallization of amphibole, garnet and plagioclase (Fig. 5a) and inconsistent with the mantle origin model.

Continental crust and its melts are generally potassium-rich (Rudnick and Gao, 2003), whereas oceanic crust and its melts usually show moderate sodium and low potassium (Martin, 1999). High Na_2O (3.8-5.1 wt.%) and MgO (1.3-3.1 wt.%) contents with Na_2O/K_2O (0.9-2.1) and $Mg^{\#}$ (46-58) values of the Aza biotite granodiorites, like

303 those of slab-derived adakitic melts ($Na_2O \geq 3.5$ wt.%, $Mg^{\#} > \sim 47$; Figs. 9a-b) (Martin,
304 1999), indicate that they were likely derived from oceanic slab rather than thickened
305 continental lower crust. Furthermore, melts derived from oceanic crust and thickened
306 lower continental crust both show high Sr/Y and $(La/Yb)_N$ ratios due to residual garnet
307 in their source. However, thickened lower continental crust-derived melts typically
308 exhibit higher Sr/Y (~30-1300) and $(La/Yb)_N$ (~20-300) ratios than oceanic crust-
309 derived melts (Sr/Y = ~25-350, $(La/Yb)_N$ = ~5-30) (Fig. 9c) (e.g., Liu et al., 2010), due
310 to the lower continental crust having higher Sr/Y (22) and La/Yb (6) ratios than the
311 oceanic crust (Sr/Y = 3, La/Yb = 0.8) (Rudnick and Gao, 2003; Sun and McDonough,
312 1989). The low Sr/Y (35.3–59.0) and $(La/Yb)_N$ ratios (5.3–17.5) of the Aza biotite
313 granodiorites thus further support derivation from partial melting of subducted oceanic
314 slab (Fig. 9c).
315 In summary, we suggest that the Aza biotite granodiorites were derived from the
316 partial melting of the subducted oceanic slab
317
318 **4.1.3 Origin of the Chango basalts**
319 The Chango basalts have high $\varepsilon_{Nd}(t)$ values (+6.4 to +7.2), similar to those of
320 the Yarlung Tsangpo ophiolites ($\varepsilon_{Nd}(t)$ = +3.3 to +9.8) (Fig. 6; Zhang et al., 2005, 2020),
321 suggesting a depleted mantle source. In addition, calculations using PRIMELT3
322 (Herzberg and Asimow, 2015) and PRIMACALC2 (Kimura and Ariskin, 2014)
323 software for Chango basalt samples with MgO > 6 wt.% yield high potential
324 temperatures of 1270-1377 °C and 1349-1393 °C (Table S5) respectively, also

supporting a source of asthenosphere with high potential temperatures of 1400 ± 200 °C (McKenzie et al., 2005).

Compared to MORB, the Chango basalts are characterized by negative Nb-Ta anomalies (Fig. 5d). Such negative Nb-Ta anomalies are commonly attributed to crustal contamination (Rudnick and Gao, 2003), crystallization of Ti-bearing minerals (e.g., rutile and Ti-bearing amphibole) (Huang et al., 2010), metasomatism by recycled terrigenous sediments (Hawkesworth et al., 1993), metasomatism by slab-derived melts (e.g., Xu et al., 2020) or hydrous fluids (e.g., Donnelly et al., 2004). The previous discussion has ruled out the influence of significant crustal contamination. Constant TiO_2 contents as MgO changes are also inconsistent with marked fractional crystallization of Ti-rich minerals (Fig. 9d). In addition, the Chango basalts have low Nb (0.86-1.47), Th (0.51-1.69 ppm) contents and Nb/La (0.08-0.16), Th/La (0.1-0.16) and Th/Yb (0.28-0.94) ratios, which suggest insignificant contribution of slab melts (Nb > 2 ppm and Nb/La > 0.5, Kepezhinskas et al., 1996) and sediment melts (Th/Yb ratios$\geqslant$2, Nebel et al., 2007; Woodhead et al., 2001) (Fig. 9e). Slab-derived hydrous fluids thus represent a potential candidate. In comparison with basalts from modern arc magmatic systems, low Th/Ce (0.04-0.06) and high $^{143}Nd/^{144}Nd$ (0.5129-0.5130) ratios of the Chango basalts are similar to those of fluid-metasomatized mantle-derived arc magmatic rocks, such as the Marianas and South Sandwich Islands (Fig. 9f; Hawkesworth et al., 1997).

In summary, the Chango basalts most probably originated from asthenospheric mantle metasomatized by slab-derived hydrous fluids.

4.2 Constraints on the timing of subduction initiation of the Neo-Tethys from magmatic rocks

Although Middle-Late Triassic magmatic rocks with arc-like composition have been identified in the southern Lhasa subblock (e.g., Huang et al., 2021; Wang et al., 2016, 2022b; Zhu et al., 2023), the timing of subduction initiation of the Neo-Tethyan slab is still controversial. This is due to the lack of typical petrological evidence for subduction initiation (e.g., boninite and fore-arc basalt), and different geodynamic models have been proposed to explain the origin of these Middle-Late Triassic arc magmatic rocks, including (1) the southward subduction of the Bangong-Nujiang Ocean (Huang et al., 2021; Zhu et al., 2011, 2013), (2) melting of previously metasomatized mantle (Dong and Zhang, 2013), and (3) the northward subduction of the Neo-Tethys Ocean (Wang et al., 2016; Zhu et al., 2023).

The Bangong-Nujiang Ocean did not subduct southwards because: (1) There is a gap in magmatic rock distribution between Qiangtang and southern Lhasa (Fig. 1b). Arc magmatic rocks, SSZ-type ophiolites, and forearc-basin sedimentary successions (Sewa Formation) all are found in Qiangtang block (Fig. 1b) (Hao et al., 2025; Ma et al., 2017). However, the northern Lhasa subblock, located south of the Bangong-Nujiang suture zone, lacks Late Triassic to Early Jurassic magmatic records related to subduction. (2) Previous studies indicate that arc magmas tend to exhibit increasingly enriched isotopic compositions as they move away from the trench, due to the increased contribution of enriched components (e.g. in U.S. Cordillera and Andes; Chapman et

al., 2017). The isotopic composition of the Middle Triassic-Early Jurassic magmatic rocks in southern Lhasa shows the characteristics of gradual enrichment from south to north (Figs. 10a-b; Tables S5, S7), which is inconsistent with southward subduction of the Bangong-Nujiang Ocean.

The lithospheric mantle metasomatized by recycled materials can be preserved for up to ~150 Myr (e.g., Lee et al., 2025). Such non-subduction-related magmatic rocks with arc-like features can therefore still be present after the closure of ocean (e.g., Mo et al., 2007), which poses a challenge for identifying past subduction events through identification of arc-like magmas. As mentioned above, the occurrence of Late Devonian-Early Carboniferous back-arc mafic magmatic rocks suggest coeval potential metasomatized mantle beneath southern Lhasa (Ma et al., 2019, 2022).

On the other hand, previous studies indicate that the period of small-scale mantle convection in subduction zones is usually less than 20 Myr (Zhou et al., 2013). Mantle convection can effectively reduce or eliminate heterogeneities of various scales within the asthenosphere (Kellogg and Turcotte, 1987; Workman and Hart, 2005). Given that asthenospheric mantle-derived Chango basalts formed 100 million years after the Late Carboniferous (353 Ma) metasomatized mantle, they are more likely to have originated from the mantle metasomatized by the subducted Neo-Tethys Ocean-derived fluids during the Late Triassic rather than earlier inherited mantle. Similarly, metasomatized depleted mantle-derived Renbu gabbro-diorites (ca. 244-238 Ma) have also been identified in southern Lhasa (Zhu et al., 2023). Therefore, the oceanic slab-derived Aza biotite granodiorites provide strong independent evidence for early

391 subduction of Neo-Tethys Ocean.

392 In conclusion, above magmatic evidence indicates that the Neo-Tethys Ocean
393 had subducted beneath the southern Lhasa subblock during the Middle-Late Triassic
394 (ca. 244-236 Ma). A coeval sudden change in magmatic component from alkaline to
395 calc-alkaline and significant increases in the water content of magma and oxygen
396 fugacity (Figs. 10c-d, 11; Tables S8-S9) are all consistent with early subduction of Neo-
397 Tethys. However, existing studies indicate that the onset of subduction may be as much
398 as ~1-7 Myr earlier than the earliest records of arc magmatic rocks (Reagan et al., 2023;
399 Wang et al., 2022b), which makes it difficult to determine the precise onset of
400 subduction.

401

402 **4.3 The subduction initiation mechanism of Neo-Tethys Ocean**

403 Determining how new subduction zones form has important implications for
404 our understanding of the driving force of plate tectonics, and Earth's tectonic history.
405 Two modes of subduction initiation (SI) are identified in both nature and models,
406 spontaneous and induced (Stern and Gerya, 2018). Any newly initiated subduction zone
407 must overcome an initial mechanical resistance (Stern and Gerya, 2018 and references
408 therein). The dynamics simulation indicates spontaneous subduction initiation is
409 intrinsically difficult, and external forces may be a necessary condition for driving
410 oceanic subduction (Crameri et al., 2020).

411 The "Tethyan one-way train" model was proposed to explain subduction
412 initiation of Neo-Tethys Ocean based on research in southern central Iran (Wan et al.,

2019). In this model, the closure of the previous ocean basin (e.g., Paleo-Tethys Ocean) provides the driving force for subduction initiation of the succeeding ocean (e.g., Neo-Tethys Ocean) (Wan et al., 2019; Zhong and Li, 2020). In Iran, subduction initiation of the Neo-Tethys Ocean and the closure of the Paleo-Tethys Ocean are thought to have occurred at the end of Triassic, based on the coupling of the earliest (200-187 Ma) arc magmas and non-conformity between continental and marine strata (228-201 Ma) (Wan et al., 2019).

However, given the vast extent (stretching 4800 km from east to west) and complex evolution of the Neo-Tethys Ocean, its subduction initiation was not necessarily synchronous. In addition, the Tibetan Plateau was formed by the amalgamation of multiple terranes different from the Zagros Plateau of Iran, which provides an opportunity to verify the "Tethyan one-way train" dynamic mechanism in a more complex system.

In Tibet, the Longmu Co-Shuanghu Ocean represents the main ocean basin of Paleo-Tethys Ocean. Existing evidence suggests that it may have closed in the Late Triassic (ca. 233-225 Ma). (1) Paleomagnetic research supports that the southern and northern Qiangtang subblocks were located at nearly the same palaeolatitudes at ca. 230 Ma (Wei et al., 2025). (2) The Upper Triassic Wanghuling Formation unconformably overlies the ophiolitic mélange (Li et al., 2007). (3) The oceanic crust eclogites in the northern part of the southern Qiangtang underwent peak metamorphism (ca. 233 Ma) and retrograde metamorphism (ca. 220 Ma) during the Late Triassic (Dan et al., 2018). The timing of the eclogite retrograde metamorphism is synchronous with

435 that of the post-collisional bimodal magmatic rocks (ca. 225-205 Ma), implying that
436 the eclogites may have experienced post-collisional exhumation during this period (Dan
437 et al., 2018). Thus, the closure of the Longmu Co-Shuanghu Ocean should have
438 occurred during the interval of 233-225 Ma (Dan et al., 2018). Accordingly, the closure
439 of the Paleo-Tethys Ocean represented by the Longmu Co-Shuanghu Ocean is later than
440 the subduction initiation of the Neo-Tethys Ocean. Furthermore, between the main
441 basins of the Paleo-Tethys Ocean and the Neo-Tethys Ocean, there are the southern
442 Qiangtang, the Lhasa blocks, and two branch ocean basins (Bangong Co-Nujiang
443 Ocean and Sumdo Ocean) (Fig. 1b). This distance makes it difficult for the closure of
444 the Longmu Co-Shuanghu Ocean to provide a remote driving force for the subduction
445 initiation of the Neo-Tethys Ocean. Numerical modeling also demonstrates that such
446 convergent force-induced subduction initiation is more likely to occur between two
447 adjacent ocean basins (Zhong and Li, 2020), as observed in Iran and Sibumasu (Wan et
448 al., 2019; Zhong and Li, 2020).

449 Based on this understanding, closure of the Sumdo Ocean, located between the
450 central and southern Lhasa subblocks, is most likely driving force for subduction of the
451 Neo-Tethys Ocean. The closure time of the Sumdo Ocean was constrained to the Middle
452 Triassic (ca. 240 Ma) by the following evidence: (1) The Sumdo eclogites in the central
453 Lhasa subblock underwent retrograde metamorphism and synchronous syn-tectonic
454 compressional deformation with their country rocks at ca. 240 Ma, indicating that they
455 probably experienced syn-collisional exhumation at this time (Li et al., 2012). (2) The
456 syn-collisional S-type granites began to form in the central Lhasa subblock at ca. 240

457 Ma (Fig. 11) (e.g., Yu, 2020). (3) The Upper Triassic Xionglai Formation
458 unconformably overlies the Late Paleozoic greenschist (Wang et al., 2024).

459 From the above, we can see that the closure of Sumdo Ocean (ca. 240 Ma) is
460 essentially contemporaneous with the earliest magmatic rocks related to subduction in
461 southern Lhasa (ca. 244-236 Ma) (Fig. 11), and this helps us to constrain subduction
462 initiation of the Neo-Tethys in Tibet. However, all these crucial magmatic rocks, such
463 as Renbu gabbros (ca. 244-238 Ma) (Zhu et al., 2023) and Aza biotite granodiorites (ca.
464 236 Ma), were dated using LA-ICP-MS with uncertainty around ~4% (2RSD) (Li et al.,
465 2015). These uncertainties might be responsible for the slight temporal differences in
466 the closure of the Sumdo Ocean and the early subduction of the Yarlung Zangbo Ocean.
467 In this case, the peak age of the normal distribution may better represent the main stage
468 of rock formation, thereby avoiding the influence of individual discrete ages. As a result,
469 we have used the method of Dan et al. (2021) to determine the peak ages for the Renbu
470 gabbros and Aza biotite granodiorites. The results indicate that the Renbu gabbros and
471 the Aza biotite granodiorites were formed around 240 Ma and 236 Ma, respectively
472 (Fig. S2). Therefore, the earliest appearance of arc-like mafic rocks and the melt of
473 subducting slabs are well aligned with the timing of closure of the Sumdo Ocean, which
474 suggests that Neo-Tethyan subduction initiation most likely occurred in the Middle
475 Triassic (ca. 240 Ma) (Fig. 12).

476 Our study supports and validates the dynamic model that the closure of an
477 adjacent ocean basin can provide the initial driving force for the initiation of the
478 subduction of the next ocean, especially for a multiple microcontinent system, like

Tibetan Plateau. In addition, the timing of initiation of Neo-Tethys Ocean subduction has been re-constrained and updated to 240 Ma, which is earlier than the reported onset time of subduction in other areas within the Neo-Tethys region. Subduction initiation of the Neo-Tethys Ocean thus may be diachronous. In future research, high-precision dating will help to constrain and understand the evolution and geodynamic processes of the Neo-Tethys. Our research also provides a reference case for the geodynamic reconstruction of other ancient subduction zones worldwide.

5 Conclusions

(1) The Aza biotite granodiorites (~236 Ma) and the Chango basalts (~219Ma) in the southern Lhasa were generated by melting of subducted oceanic slab and metasomatized asthenospheric mantle, respectively.

(2) The Neo-Tethys Ocean may have begun to subduct northward around 240 Ma and formed widespread Middle-Late Triassic magmatic rocks distributed throughout southern Tibet.

(3) The convergent force generated by the closure of the Sumdo Ocean may well have provided the driving force for the subduction initiation of the Neo-Tethys Ocean.

Acknowledgments

We thank editor in chief Prof. Di-Cheng Zhu and three anonymous reviewers for their valuable suggestions and comments that helped us improve the paper

substantially. We appreciate the assistance of Xin-Yu Wang, Sheng–Ling Sun, Ze-Xian Cui, Jin–Long Ma, Guan-Hong Zhu, Xiang–Lin Tu and Pan Qu for zircon age and whole rock geochemical analyses. Financial support was provided by the Deep Earth Probe and Mineral Resources Exploration-National Science and Technology Major Project of China (No. 2024ZD1001103), the National Natural Science Foundation of China (grant 42122022), the Strategic Priority Research Program (B) of the Chinese Academy of Sciences (grant XDB0840300) and the National Key Research and Development Program of China (grant 2024YFC2909903).

Data availability statement

The research data associated with the manuscript are listed in the supporting information.

References

Castillo, P.R., Janney, P.E., Solidum, R.U., 1999. Petrology and geochemistry of Camiguin Island, southern Philippines: insights to the source of adakites and other lavas in a complex arc setting. Contributions to Mineralogy and Petrology 134(1), 33-51. https://doi.org/10.1007/s004100050467.

Chapman, J.B., Ducea, M.N., Kapp, P., Gehrels, G.E., DeCelles, P.G., 2017. Spatial and temporal radiogenic isotopic trends of magmatism in Cordilleran orogens. Gondwana Research 48, 189-204. https://doi.org/10.1016/j.gr.2017.04.019.

Crameri, F., Magni, V., Domeier, M., Shephard, G.E., Chotalia, K., Cooper, G., Eakin,

C.M., Grima, A.G., Gürer, D., Király, Á., Mulyukova, E., Peters, K., Robert, B., Thielmann, M., 2020. A transdisciplinary and community-driven database to unravel subduction zone initiation. Nature Communications 11, 3750. https://doi.org/10.1038/s41467-020-17522-9.

Dai, J., Wang, C., Polat, A., Santosh, M., Li, Y., Ge, Y., 2013. Rapid forearc spreading between 130 and 120Ma: Evidence from geochronology and geochemistry of the Xigaze ophiolite, southern Tibet. Lithos 172-173, 1-16. https://doi.org/10.1016/j.lithos.2013.03.011.

Dan, W., Wang, Q., Murphy, J.B., Zhang, X.Z., Xu, Y.G., White, W.M., Jiang, Z.Q., Ou, Q., Hao, L.L., Qi, Y., 2021. Short duration of Early Permian Qiangtang-Panjal large igneous province: Implications for origin of the Neo-Tethys Ocean. Earth and Planetary Science Letters 568, 117054. https://doi.org/10.1016/j.epsl.2021.117054.

Dan, W., Wang, Q., White, W.M., Zhang, X.Z., Tang, G.J., Jiang, Z.Q., Hao, L.L., Ou, Q., 2018. Rapid formation of eclogites during a nearly closed ocean: Revisiting the Pianshishan eclogite in Qiangtang, central Tibetan Plateau. Chemical Geology 477, 112-122. https://doi.org/10.1016/j.chemgeo.2017.12.012.

Defant, M.J., Drummond, M.S., 1990. Derivation of some modern arc magmas by melting of young subducted lithosphere. Nature 347, 662–665. https://doi.org/10.1038/347662a0.

Dong, X., Zhang, Z.M., 2013. Genesis and tectonic significance of the Early Jurassic magmatic rocks from the southern Lhasa terrane. Acta Petrologica Sinica. 29

(6), 1933–1948 (in Chinese with English abstract).

Dong, X., Zhang, Z.M., Santosh, M., 2010. Zircon U–Pb chronology of the Nyingtri Group, Southern Lhasa Terrane, Tibetan Plateau: implications for Grenvillian and Pan-African Provenance and Mesozoic–Cenozoic metamorphism. Journal of Geology 118, 677–690.

Donnelly, K.E., Goldstein, S.L., Langmuir, C.H., Spiegelman, M., 2004. Origin of enriched ocean ridge basalts and implications for mantle dynamics. Earth and Planetary Science Letters 226(3-4), 347-366. https://doi.org/10.1016/j.epsl.2004.07.019.

Ge, R.F., Wilde, S.A., Zhu, W.B., Wang, X.L., 2023. Earth's early continental crust formed from wet and oxidizing arc magmas. Nature 623, 334-339. https://doi.org/10.1038/s41586-023-06552-0.

Hao, L.L., Hu, W.L., Wang, Q., Kerr, A.C., Dan, W., Zhang, X.Z., Yang, Z.Y., Sun, P., 2025. Bangong-Nujiang Neo-Tethyan Ocean (Central Tibet): Geodynamics, crustal evolution, metallogeny, and linkages to the “Yanshan Movement”. Earth-Science Reviews 265, 105119.

Hastie, A.R., Kerr, A.C., Pearce, J.A., Mitchell, S.F., 2007. Classification of altered volcanic island arc rocks using immobile trace elements: Development of the Th–Co discrimination diagram. Journal of Petrology 48(12), 2341-2357. https://doi.org/10.1093/petrology/egm062.

Hawkesworth, C.J., Gallagher, K., Hergt, J.M., McDermott, F., 1993. Mantle and slab contributions in arc magmas. Annual Review of Earth and Planetary Sciences

21, 175–204. https://doi.org/10.1146/annurev.ea.21.050193.001135.

Hawkesworth, C.J., Turner, S.P., McDermott, F., Peate, D.W., van Calsteren, P., 1997. U-Th Isotopes in Arc Magmas: Implications for Element Transfer from the Subducted Crust. Science 276(5312), 551-555.

Herzberg, C., Asimow, P.D., 2015. PRIMELT3 MEGA.XLSM software for primary magma calculation: Peridotite primary magma MgO contents from the liquidus to the solidus. Geochem. Geophys. Geosyst 16, 563 – 578. https://doi:10.1002/2014GC005631.

Hoskin, P.W.O., Black, L.P., 2000. Metamorphic zircon formation by solid-state recrystalli-zation of protolith igneous zircon. Journal of Metamorphic Geology 18(4), 423-439. https://doi.org/10.1046/j.1525-1314.2000.00266.x.

Huang, T.Y., Wang, Q., Wyman, D.A., Ma, L., Tang, G.J., Zhang, Z.P., Dong, H., 2022. Subduction Erosion Revealed by Late Mesozoic Magmatism in the Gangdese Arc, South Tibet. Geophysical Research Letters 49, e2021GL097360. https://doi.org/10.1029/2021GL097360.

Huang, X.L., Niu, Y.L., Xu, Y.G., Chen, L.L., Yang, Q.J., 2010. Mineralogical and geochemical constraints on the petrogenesis of post-collisional potassic and ultrapotassic rocks from Western Yunnan, SW China. Journal of Petrology 51(8), 1617-1654. https://doi.org/10.1093/petrology/egq032.

Huang, Y., Ren, M.H., Jowitt, S.M., Li, G.M., Fu, J.G., Zhang, Z., Lang, X.H., Liu, H., Zhang, L., 2021. Middle Triassic arc magmatism in the southern Lhasa terrane: Geochronology, petrogenesis and tectonic setting. Lithos 380-381, 105857.

https://doi.org/10.1016/j.lithos.2020.105857.

Kang, Z.Q., Xu, J.F., Wilde, S.A., Feng, Z.H., Chen, J.L., Wang, B.D., Fu, W.C., Pan, H.B., 2014. Geochronology and geochemistry of the Sangri group volcanic rocks, southern Lhasa Terrane: implications for the early subduction history of the Neo-Tethys and Gangdese magmatic arc. Lithos 200, 157–168. https://doi.org/10.1016/j.lithos.2014.04.019.

Kellogg, L.H., Turcotte, D.L., 1987. Homogenization of the mantle by convective mixing and diffusion. Earth and Planetary Science Letters 81, 371-378. https://doi.org/10.1016/0012-821X(87)90124-5.

Kepezhinskas, P., Defant, M.J., Drummond, M.S., 1996. Progressive enrichment of island arc mantle by melt-peridotite interaction inferred from Kamchatka xenoliths. Geochimica et Cosmochimica Acta 60(7), 1217-1229. https://doi.org/10.1016/0016-7037(96)00001-4.

Kimura, J.I., Ariskin, A.A., 2014. Calculation of water-bearing primary basalt and estimation of source mantle conditions beneath arcs: PRIMACALC2 model for WINDOWS. Geochemistry, Geophysics, Geosystems 15, 1494-1514. http://doi.org/10.1002/2014GC005329.

Leake, B.E., Wooooey, A.R., Birch, W.D., Gilbert, M.C., Grice, J.D., Hawthorne, F.C., Kato, A., Kisch, H.J., Krivovichev, V.G., Linthout, K., Laird, J., Mandarino, J., Maresch, M.V., Nickel, E.H., Rock, N.M.S., Schumacher, J.C., Smith, D.C., Stephenson, N.C.N., Ungaretti, L., Whittaker, E.J.W., Youzhi, G., 1997. Nomenclature of amphiboles-Report of the subcommittee on amphiboles of the

611 International Mineralogical Association Commission on New Minerals and
612 Mineral Names. European Journal of Mineralogy. 9 (3), 623-651.
613 https://doi.org/10.1180/minmag.1997.061.405.13.
614 Lee, W., Kim, D., Oh, J., Kim, J., Kim, C.H., Park, C.H., Kim, J.M., Lee, Y., Lee, H.,
615 2025. Metasomatized lithospheric mantle as a reservoir for recycled volatiles:
616 Noble gas and oxygen isotope systematics in the East Sea. Geochimica et
617 Cosmochimica Acta. https://doi.org/10.1016/j.gca.2025.12.037.
618 Li, C., Zhai, Q.G., Dong, Y.S., Yu, J.J., Huang, X.P., 2007. Establishment of the Upper
619 Triassic Wanghuling Formation at Guoganjianian Mountain, central Qiangtang,
620 Qinghai–Tibet Plateau, and its significance. Geological Bulletin of China 26,
621 1003–1008 (in Chinese with English abstract).
622 Li, H.Q., Xu, Z..Q., Yang, J.S., Tang, Z.M., 2012. Indosinian Orogenesis in the Lhasa
623 Terrane, Tibet: New Muscovite 40Ar-39Ar Geochronology and Evolutionary
624 Process. Acta Geologica Sinica - English Edition 86(5), 1116-1127.
625 https://doi.org/10.1111/j.1755-6724.2012.00735.x.
626 Li, X.H., Liu, X.M., Liu, Y.S., Su, L., Sun, W.D., Huang, H.Q., Yi, K., 2015. Accuracy
627 of LA-ICPMS zircon U-Pb age determination: an inter-laboratory comparison.
628 Sci. China Earth Sci 58, 1722–1730.
629 Liu, F., Yang, J.S., Lian, D.Y., Li, G.L., 2020. Geological features of Neothyan
630 ophiolites in Tibetan Plateau and its tectonic evolution. Acta Petrol. Sin 36(10),
631 2913-2945 (in Chinese with English abstract).
632 Liu, S.A., Li, S.G., He, Y.S., Huang, F., 2010. Geochemical contrasts between early

633 Cretaceous ore-bearing and orebarren high-Mg adakites in central-eastern
634 China: Implications for petrogenesis and Cu-Au mineralization. Geochimica et
635 Cosmochimica Acta 74, 7160–7178. https://doi.org/10.1016/j.gca.2010.09.003.
636 Ma, A., Hu, X., Garzanti, E., Han, Z., Lai, W., 2017. Sedimentary and tectonic evolution
637 of the southern Qiangtang basin: Implications for the Lhasa-Qiangtang collision
638 timing. Journal of Geophysical Research: Solid Earth 122(7), 4790-4813.
639 https://doi.org/10.1002/2017JB014211.
640 Ma, L., Kerr, A.C., Wang, Q., Jiang, Z.-Q., Tang, G.J., Yang, J.H., Xia, X.P., Hu, W.L.,
641 Yang, Z.Y., Sun, P., 2019. Nature and Evolution of Crust in Southern Lhasa,
642 Tibet: Transformation From Microcontinent to Juvenile Terrane. Journal of
643 Geophysical Research: Solid Earth 124(7), 6452-6474.
644 https://doi.org/10.1029/2018JB017106.
645 Ma, L., Wang, Q., Tang, G.J., Li, C., 2022. Nature and Evolution of Crust in the
646 Southern Lhasa During Phanerozoic. Geotectonica et Metallogenia 46(06),
647 1170-1184 (in Chinese with English abstract).
648 Macpherson, C.G., Dreher, S.T., Thirlwall, M.F., 2006. Adakites without slab melting:
649 High pressure differentiation of island arc magma, Mindanao, the Philippines.
650 Earth and Planetary Science Letters 243(3-4), 581-593.
651 https://doi.org/10.1016/j.epsl.2005.12.034.
652 Maniar, P.D., Piccoli, P.M., 1989. Tectonic discrimination of granitoids. Geological
653 Society of America Bulletin 101(5), 635-643. https://doi.org/10.1130/0016-
654 7606(1989)101<0635:TDOG>2.3.CO;2.

655 Martin, H., 1999. Adakitic magmas: modern analogues of Archean granitoids. Lithos
656 46(3), 411–429. https://doi.org/10.1016/S0024-4937(98)00076-0.
657 McKenzie, D., Jackson, J., Priestley, K., 2005. Thermal structure of oceanic and
658 continental lithosphere. Earth and Planetary Science Letters 233(3), 337–349.
659 https://doi.org/10.1016/j.epsl.2005.02.005.
660 Nebel, O., Münker, C., Nebel-Jacobsen, Y.J., Kleine, T., Mezger, K., Mortimer, N.,
661 2007. Hf–Nd–Pb isotope evidence from Permian arc rocks for the long-term
662 presence of the Indian–Pacific mantle boundary in the SW Pacific. Earth and
663 Planetary Science Letters 254(3-4), 377–392.
664 https://doi.org/10.1016/j.epsl.2006.11.046.
665 Niu, Y., Batiza, R., 1997. Trace element evidence from seamounts for recycled oceanic
666 crust in the eastern equatorial Pacific mantle. Earth and Planetary Science
667 Letters 148(3-4), 471–484. https://doi.org/10.1016/S0012-821X(97)00048-4.
668 Pearce, J.A., Thirlwall, M.F., Ingram, G., Murton, B.J., Arculus, R.J., Van der Laan,
669 S.R., 1992. Isotopic evidence for the origin of boninites and related rocks drilled
670 in the Izu-Bonin (Ogasawara) forearc, Leg 1251. Proc. Ocean Drilling Program.
671 Scientific Results 125, 237–261.
672 Plank, T., Langmuir, C.H., 1998. The chemical composition of subducting sediment and
673 its consequences for the crust and mantle. Chemical Geology 145(3-4), 325–
674 394. https://doi.org/10.1016/S0009-2541(97)00150-2.
675 Polat, A., Hofmann, A.W., Rosing, M.T., 2002. Boninite-like volcanic rocks in the 3.7–
676 3.8 Ga Isua greenstone belt, West Greenland: geochemical evidence for intra-

677 oceanic subduction zone processes in the early Earth. Chemical Geology 184(3-
678 4), 231-254. https://doi.org/10.1016/S0009-2541(01)00363-1.
679 Rapp, R.P., Shimizu, N., Norman, M.D., Applegate, G.S., 1999. Reaction between slab-
680 derived melts and peridotite in the mantle wedge: experimental constraints at
681 3.8 Gpa. Chemical Geology 160(4), 335–356. https://doi.org/10.1016/S0009-
682 2541(99)00106-0.
683 Reagan, M.K., Pearce, J.A., Shervais, J.W., Christeson, G.L., 2023. Subduction
684 initiation as recorded in the Izu-Bonin-Mariana forearc. Earth-Science Reviews
685 246, 104573. https://doi.org/10.1016/j.earscirev.2023.104573.
686 Ridolfi, F., Renzulli, A., Puerini, M., 2010. Stability and chemical equilibrium of
687 amphibole in calc-alkaline magmas: an overview, new thermobarometric
688 formulations and application to subduction-related volcanoes. Contributions to
689 Mineralogy and Petrology 160(1), 45-66. http://doi.org/10.1007/s00410-009-
690 0465-7.
691 Rudnick, R.L., Gao, S., 2003. Composition of the Continental Crust. In: Holland, H.D.,
692 Turekian, K.K. (Eds.), The Crust: Treatise on Geochemistry: Amsterdam, 3, 1-
693 64. https://doi.org/10.1016/B0-08-043751-6/03016-4.
694 Stern, C.R., Kilian, R., 1996. Role of the subducted slab, mantle wedge and continental
695 crust in the generation of adakites from the Andean Austral Volcanic Zone.
696 Contributions to Mineralogy and Petrology 123(3), 263-281.
697 https://doi.org/10.1007/s004100050155.
698 Stern, R.J., Gerya, T., 2018. Subduction initiation in nature and models: a review.

699 Tectonophysics 746, 173–198.
700 Sun, S.S., McDonough, W.F., 1989. Chemical and isotopic systematics of oceanic
701 basalts: implications for mantle composition and processes. Geological Society,
702 London, Special Publications 42(1), 313–345.
703 https://doi.org/10.1144/GSL.SP.1989.042.01.19.
704 Tian, Y.M., Huang, F., Xu, J.F., Zeng, Y.C., Hu, P., Yu, H.X., Tian, Y., Yang, Z.Y., Yang,
705 X.L., 2022. Petrogenesis and geodynamic mechanisms of the Late Cretaceous
706 magmatic 'flare-up' in the southern Lhasa Terrane, Tibet. Lithos 424-425,
707 106766. https://doi.org/10.1016/j.lithos.2022.106766.
708 Valley, J.W., 2003. Oxygen isotopes in zircon. Reviews in Mineralogy and
709 Geochemistry 53(1), 343–385. https://doi.org/10.2113/0530343.
710 Vervoort, J.D., Blichert-Toft, J., 1999. Evolution of the depleted mantle: Hf isotope
711 evidence from juvenile rocks through time. Geochimica et Cosmochimica Acta
712 63, 533–556. https://doi.org/10.1016/S0016-7037(98)00274-9.
713 Wan, B., Wu, F.Y., Chen, L., Zhao, L., Liang, X.F., Xiao, W.J., Zhu, R.X., 2019.
714 Cyclical one-way continental rupture-drift in the Tethyan evolution. Subduction
715 driven plate tectonics. Science China Earth Sciences 49(12), 2004–2017 (in
716 Chinese with English abstract).
717 Wang, B., Xie, C.M., Zhao, G.C., Yakymchuk, C., Dong, Y.S., Song, Y.H., 2024. Initial
718 sedimentation after the closure of the Sumdo Paleo-Tethys Ocean: Implications
719 for early Mesozoic tectonics in the East Tethys domain. Lithos 480-481, 107668.
720 https://doi.org/10.1016/j.lithos.2024.107668.

721 Wang, C., Ding, L., Zhang, L.Y., Kapp, P., Pullen, A., Yue, Y.H., 2016. Petrogenesis of
722 Middle–Late Triassic volcanic rocks from the Gangdese belt, southern Lhasa
723 terrane: Implications for early subduction of Neo-Tethyan oceanic lithosphere.
724 Lithos 262, 320-333. https://doi.org/10.1016/j.lithos.2016.07.021.
725 Wang, J.G., Yang, F., Santosh, M., Zhang, X.Q., Wei, W.T., Zhuan, S.P., Zhang, J.Q.,
726 Chen, C., Wang, S., Yang, X.P., Xue, F., 2022a. Middle Triassic volcanic rocks
727 from the Gangdese belt, southern Tibet: petrogenesis and implications for
728 Tethys tectonic evolution. International Geology Review 64(6), 867-884.
729 https://doi.org/10.1080/00206814.2021.1891468.
730 Wang, Q., Xu, J.F., Jian, P., Bao, Z.W., Zhao, Z.H., Li, C.F., Xiong, X.L., Ma, J.L., 2006.
731 Petrogenesis of adakitic porphyries in and extensional tectonic setting, Dexing,
732 South China: implications for the Genesis of porphyry copper mineralization.
733 Journal of Petrology 47(1), 119–144. https://doi.org/10.1093/petrology/egi070.
734 Wang, X.H., Lang, X.H., Klemd, R., Deng, Y.L., Tang, J.X., 2022b. Subduction
735 initiation of the Neo-Tethys oceanic lithosphere by collision-induced
736 subduction transference. Gondwana Research 104, 54-69.
737 https://doi.org/10.1016/j.gr.2021.08.012.
738 Wang, X.H., Lang, X.H., Tang, J.X., Deng, Y.L., Cui, Z.W., 2019. Early–Middle
739 Jurassic (182–170 Ma) Ruocuo adakitic porphyries, southern margin of the
740 Lhasa terrane, Tibet: Implications for geodynamic setting and porphyry Cu–Au
741 mineralization. Journal of Asian Earth Sciences 173, 336-351.
742 https://doi.org/10.1016/j.jseaes.2019.01.042.

743 Wang, Z.Z., Dong, M.C., Zhao, Z.D., Li, X.P., Liu, D., Wang, Q., Zhu, D.C., Zhang,
744 L.L., Mo, X.X., Meng, Y.K., Cong, F.Y., Sheikh, Land Lutfi, W., 2022c. High-
745 and low-Mg adakitic rocks in southern Tibet: Implication for the crustal
746 thickening and geodynamic process in the late Cretaceous. Lithos 422-423,
747 106748. https://doi.org/10.1016/j.lithos.2022.106748.
748 Wei, B., Cheng, X., Domeier, M., Yang, P., Li, S., Xing, L., Jiang, N., Zhang, W., Zhang,
749 J., Shen, Z., Chen, Q., Zhang, D., Zhang, M., Zhou, Y., Deng, C., Wu, H., 2025.
750 A Cimmerian keystone: Middle-late Triassic paleomagnetic and calcite
751 geochronologic constraints on the South Qiangtang Block. Earth and Planetary
752 Science Letters 664, 119442. https://doi.org/10.1016/j.epsl.2025.119442.
753 Wen, D.R., Liu, D.Y., Chung, S.L., Chu, M.F., Ji, J.Q., Zhang, Q., Song, B., Lee, T.Y.,
754 Yeh, M.W., Lo, C.H., 2008. Zircon SHRIMP U–Pb ages of the Gangdese
755 batholith and implications for Neotethyan subduction in southern Tibet.
756 Chemical Geology 252, 191–201.
757 Winchester, J.A., Floyd, P.A., 1977. Geochemical discrimination of different magma
758 series and their differentiation products using immobile elements. Chemical
759 Geology 20, 325–343. https://doi.org/10.1016/0009-2541(77)90057-2.
760 Wood, D.A., Joron, J.L., Treuil, M., 1979. Are-appraisal of the use of trace elements to
761 classify and discriminate between magma series erupted in different tectonic
762 settings. Earth and Planetary Science Letters 45(2), 326-336.
763 https://doi.org/10.1016/0012-821X(79)90133-X.
764 Woodhead, J.D., Hergt, J.M., Davidson, J.P., Eggins, S.M., 2001. Hafnium isotope

765 evidence for conservative element mobility during subduction zone processes.
766 Earth and Planetary Science Letters 192(3), 331–346.
767 https://doi.org/10.1016/S0012-821X(01)00453-8.
768 Workman, R.K., Hart, S.R., 2005. Major and trace element composition of the depleted
769 MORB mantle (DMM). Earth and Planetary Science Letters 231(1-2), 53-72.
770 https://doi.org/10.1016/j.epsl.2004.12.005.
771 Xiong, Q., Griffin, W.L., Zheng, J.-P., O'Reilly, S.Y., Pearson, N.J., Xu, B., Belousova,
772 E.A., 2016. Southward trench migration at ~130–120 Ma caused accretion of
773 the Neo-Tethyan forearc lithosphere in Tibetan ophiolites. Earth and Planetary
774 Science Letters 438, 57-65. https://doi.org/10.1016/j.epsl.2016.01.014.
775 Xu, Y.G., Wang, Q., Tang, G.J., Wang, J., Li, H.Y., Zhou, J.S., Li, Q.W., Qi, Y., Liu, P.P.,
776 Ma, L., Fan, J.J., 2020. The origin of arc basalts: New advances and remaining
777 questions. Science China Earth Sciences 63(12), 1969-1991.
778 Yang, J.S., Xu, Z.Q., Li, Z.L., Xu, X.Z., Li, T.F., Ren, Y.F., Li, H.Q., Chen, S.Y.,
779 Robinson, P.T., 2009. Discovery of an eclogite belt in the Lhasa block, Tibet: a
780 new border for Paleo-Tethys? Journal of Asian Earth Sciences 34, 76–89.
781 Yin, A., Harrison, T.M., 2000. Geologic Evolution of the Himalayan-Tibetan Orogen.
782 Annual Review of Earth and Planetary Sciences 28, 211-280.
783 https://doi.org/10.1146/annurev.earth.28.1.211.
784 Yu, Y.P., 2020. Permian-Jurassic magmatism and its tectonic significance in Sumdo area
785 southern Tibet. Jilin University, Jilin (120 pp.).
786 Zhang, S.Q., Mahoney, J., Mo, X.X., Ghazi, A., Milani, L., Crawford, A., Guo, T.Y.,

787 Zhao, Z.D., 2005. Evidence for a widespread Tethyan upper mantle with Indian-
788 Ocean-type isotopic characteristics. Journal of Petrology 46(4), 829-858.
789 https://doi.org/10.1093/petrology/egi002.
790 Zhang, Y.C., Li, X.P., Ma, S.T., Du, L., Wang, X.M., Kong, F.M., Wei, G.D., Zhang,
791 S.K., Schertl, H.P., 2020. Sr-Nd isotopic study of amphibolite in Xigaze
792 ophiolite, southern Tibet. Journal of Shandong University of Science and
793 Technology (Natural Science) 39(02), 1-11(in Chinese with English abstract).
794 Zhong, X., Li, Z.H., 2020. Subduction initiation during collision-induced subduction
795 transference: Numerical modeling and implications for the Tethyan evolution.
796 Journal of Geophysical Research: Solid Earth 125(2), e2019JB019288.
797 https://doi.org/10.1029/2019JB019288.
798 Zhou, X.L., Liu, H., Zhao, C.C., 2013. The Small-Scale Mantle Convection and the
799 Correlating with Sequence Stratigraphic. Advances in Geosciences 3, 299-307
800 (in Chinese with English abstract).
801 Zhu, D.C., Mo, X.X., Niu, Y.L., Zhao, Z.D., Wang, L.Q., Pan, G.T., Wu, F.Y., 2009.
802 Zircon U-Pb dating and in-situ Hf isotopic analysis of Permian peraluminous
803 granite in the Lhasa terrane, southern Tibet: implications for Permian collisional
804 orogeny and paleogeography. Tectonophysics 469, 48–60.
805 Zhu, D.C., Pan, G.T., Chung, S.L., Liao, Z.L., Wang, L.Q., Li, G.M., 2008. SHRIMP
806 Zircon Age and Geochemical Constraints on the Origin of Lower Jurassic
807 Volcanic Rocks from the Yeba Formation, Southern Gangdese, South Tibet.
808 International Geology Review 50(5), 442-471. https://doi.org/10.2747/0020-

6814.50.5.442.

Zhu, D.C., Wang, Q., Weinberg, R.F., Cawood, P.A., Zhao, Z., Hou, Z.Q., Mo, X.X., 2023. Continental crustal growth processes recorded in the Gangdese Batholith, southern Tibet. Annu. Rev. Earth Planet. Sci 51(1), 155 – 188. https://doi.org/10.1146/annurev-earth-032320-110452.

Zhu, D.C., Zhao, Z.D., Niu, Y.L., Dilek, Y., Hou, Z.Q., Mo, X.X., 2013. The origin and pre-Cenozoic evolution of the Tibetan Plateau. Gondwana Research 23(4), 1429-1454. https://doi.org/10.1016/j.gr.2012.02.002.

Zhu, D.C., Zhao, Z.D., Niu, Y.L., Mo, X.X., Chung, S.L., Hou, Z.Q., Wang, L.Q., Wu, F.Y., 2011. The Lhasa Terrane: Record of a microcontinent and its histories of drift and growth. Earth and Planetary Science Letters 301(1-2), 241-255. https://doi.org/10.1016/j.epsl.2010.11.005.

Zhu, R.X., Zhao, P., Zhao, L., 2022. Tectonic evolution and geodynamics of the Neo-Tethys Ocean. Science China Earth Sciences 65(1), 1 – 24. https://doi.org/10.1007/s11430-021-9845-7.

Figure captions

Fig. 1. (a) Tectonic framework of the Tibetan Plateau showing the major tectonic subdivisions, and distribution of suture zones; (b) Geological map of the central-southern Tibetan Plateau (modified after Ma et al., 2019). A compilation of locations of the Permian-Triassic magmatic rocks in the central-southern Tibetan Plateau is given in Table S1. (c) Simplified geological map of the study area (modified from 1:250,000

831 geologic map). Abbreviations: KF = Karakorum Fault; KKF = Karakax Fault; ATF =
832 Altyn Tagh Fault; NQSZ = North Qilian Suture Zone; SQSZ = South Qilian Suture
833 Zone; KSZ = Kunlun Suture Zone; KLF = Kunlun Fault; XFS = Xianshuihe Fault
834 System; JSSZ = Jinshajiang Suture Zone; LSSZ = Longmu Co-Shuanghu Suture Zone;
835 BNSZ = Bangong-Nujiang Suture Zone; SNMZ = Shiquanhe Namco ophiolite
836 Mélange Zone; LMF = Luobadui-Milashan Fault; YZSZ = Yarlung–Zangbo Suture
837 Zone; IBR = Indo-Burmese Ranges; RRF = Red River Fault; SF = Sagaing Fault.
838
839 **Fig. 2.** Representative field photographs of (a) the Aza biotite granodiorites and (b) the
840 Chango basalts; Photomicrographs of (c and d) biotite granodiorites and (e and f)
841 basalts. Mineral abbreviations: Cpx—clinopyroxene; Pl—plagioclase; Qz—quartz;
842 Amp—amphibolite; Bt—biotite; Act—actinolite.
843
844 **Fig. 3.** LA-ICP-MS and SIMS zircon U-Pb concordia diagrams with
845 cathodoluminescence images for (a) 21AZ05-1 (biotite granodiorite) and (b) 21CG04-
846 1 (basalt). Figure b shows inherited zircons (left) and magmatic zircons (right). LA-
847 ICP-MS = Laser ablation inductively coupled plasma mass spectrometer; SIMS =
848 secondary ion mass spectrometer.
849
850 **Fig. 4.** (a) SiO_2 vs. Nb/Y diagram (after Winchester and Floyd, 1977). (b) Th vs. Co
851 diagram (after Hastie et al., 2007). (c) A/NK vs A/CNK diagram (after Maniar and
852 Piccoli, 1989). (d) Sr/Y vs. Y diagram (after Defant and Drummond, 1990). Data

853 sources: Sangri Group basalts (Kang et al., 2014; Wang et al., 2016).

854

855 **Fig. 5.** Chondrite-normalized REE and primitive-mantle-normalized trace element
856 patterns for samples: (a) and (b) are Aza biotite granodiorites, (c) and (d) are Chango
857 basalts. Normalised data are from Sun and McDonough (1989). The data for Sangri
858 Group basalts are from Kang et al. (2014); Wang et al. (2016).

859

860 **Fig. 6.** Plot of initial $\varepsilon_{Nd}(t)$ vs. $^{87}Sr/^{86}Sr$ for samples. Data sources are as follows: Neo-
861 Tethys ophiolites (Zhang et al., 2005, 2020). Subducted Neo-Tethys oceanic slab-
862 derived adakites (Tian et al., 2022; Wang et al., 2019, 2022c). Sangri Group basalts
863 (Kang et al., 2014; Wang et al., 2016). Yeba Formation basalts (Zhu et al., 2008).

864

865 **Fig. 7.** Elements versus Zr correlation diagrams for Chango basalts.

866

867 **Fig. 8.** (a) Whole-rock ε_{Nd} (t) vs. SiO_2 diagram. (b) Whole-rock $(^{87}Sr/^{86}Sr)_i$ vs. SiO_2
868 diagram. (c) Whole-rock ε_{Nd} (t) vs. $^{147}Sm/^{144}Nd$ diagram. (d) Whole-rock ε_{Nd} (t) vs.
869 MgO diagram.

870

871 **Fig. 9.** (a) MgO vs. SiO_2 diagram. (b) $Mg^{\#}$ vs. SiO_2 diagram. Mantle assimilation curve
872 is after Rapp et al. (1999) (Curve 1); the proportion of assimilated peridotite is also
873 shown. The crustal AFC curve is after Stern and Kilian (1996). The starting point of
874 Curve 1 represents the composition of a metabasaltic or eclogite experimental melt,

which is not hybridized with peridotite (Rapp et al., 1999). The fields of subducted oceanic crust-, subducted continental crust-and thickened lower crust-derived adakites are after Wang et al. (2006). Data for metabasalt and eclogite experimental melts (1–4 GPa) are from Rapp et al. (1999) and references therein. (c) Sr/Y vs. $(La/Yb)_N$ diagram (after Liu et al., 2010). (d) TiO_2 vs. MgO diagram. (e) Th/La vs. Th diagram. (f) Th/Ce vs. $^{143}Nd/^{144}Nd$ diagram (after Hawkesworth et al., 1997). The data for marine sediments are from Plank and Langmuir (1998). MORB data are from Niu and Batiza (1997).

Fig. 10. (a) Latitude vs. $\varepsilon_{Hf}(t)$ diagram. (b) Latitude vs. $\varepsilon_{Nd}(t)$ diagram. (c) H_2O_{melt} vs. Age diagram. (d) ΔFMQ vs. Age diagram. The $\varepsilon_{Hf}(t)$ data of ~244-201 Ma intermediate-felsic rocks are provided in Table S7. The $\varepsilon_{Nd}(t)$ data of ~244-174 Ma mafic rocks are provided in Table S5. The calculation results of water content and oxygen fugacity of magmatic rocks are provided in Table S8. The calculation methods of water content and oxygen fugacity of magmatic rocks are from Ge et al. (2023) and Ridolfi et al. (2010).

Fig. 11. (a) Age histograms of Permian-Triassic magmatic rocks and collisional metamorphic rocks in the central Lhasa subblock. (b) Age histograms of Permian-Triassic magmatic rocks in the southern Lhasa subblock. The age data for magmatic and metamorphic rocks are provided in Table S9.

Fig. 12. Schematic illustrations of early evolution of the Neo-Tethys Ocean. The process can be summarized as follows: The closure of the Sumdo Tethyan Ocean during the Middle Triassic (ca. 240 Ma) resulted in the collision between the central and southern Lhasa subblocks. Meanwhile, the continuously generated convergent forces during the collision were released along the weak zone (e.g., the ocean-continent transition zone) on the southern margin of the southern Lhasa subblock, leading to the formation of the Neo-Tethys Ocean subduction zone and thus triggering extensive Middle-Late Triassic magmatism in southern Lhasa.

Figure 1

Click here to access/download;Figure;Figure 1.pdf

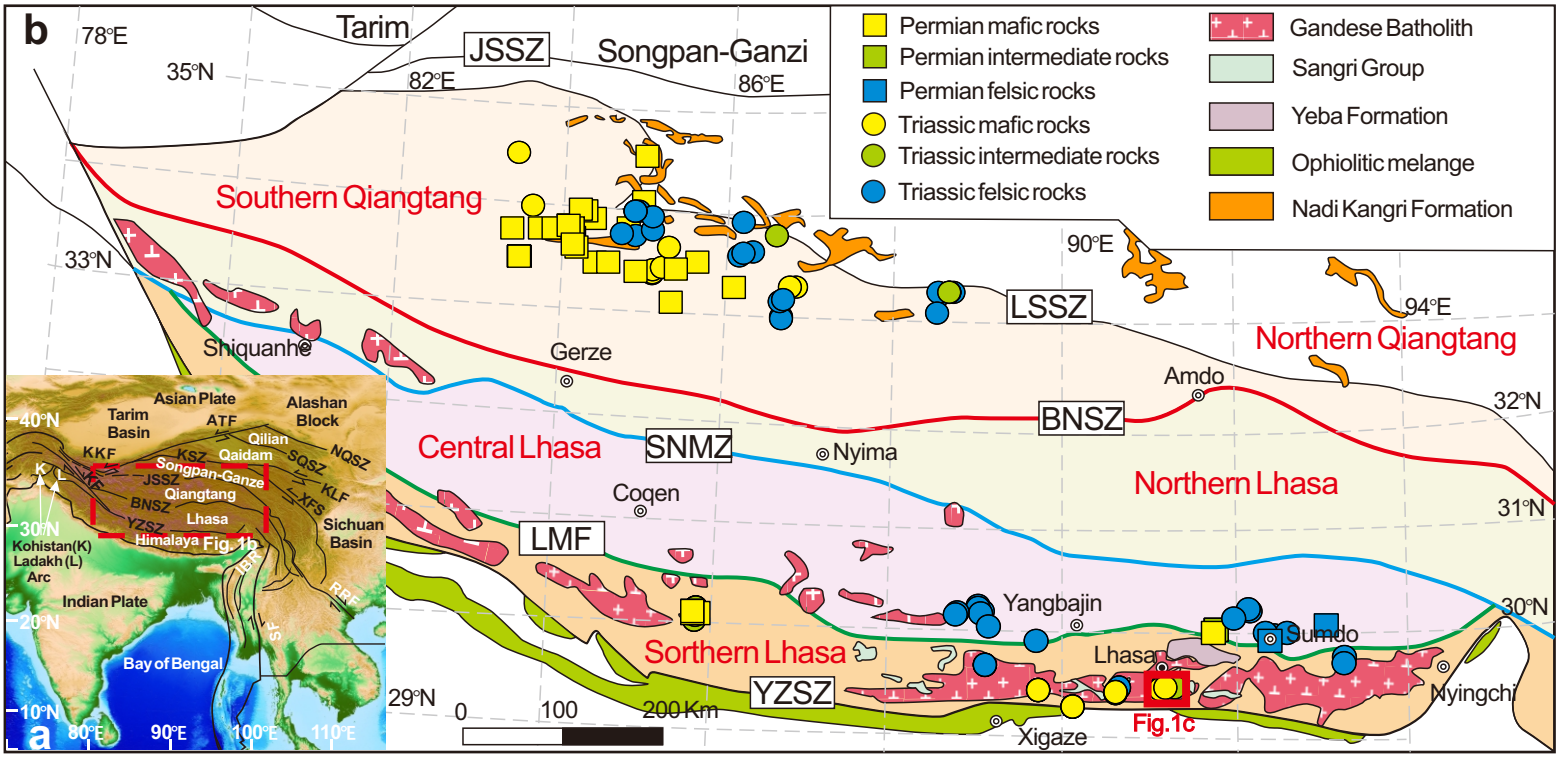

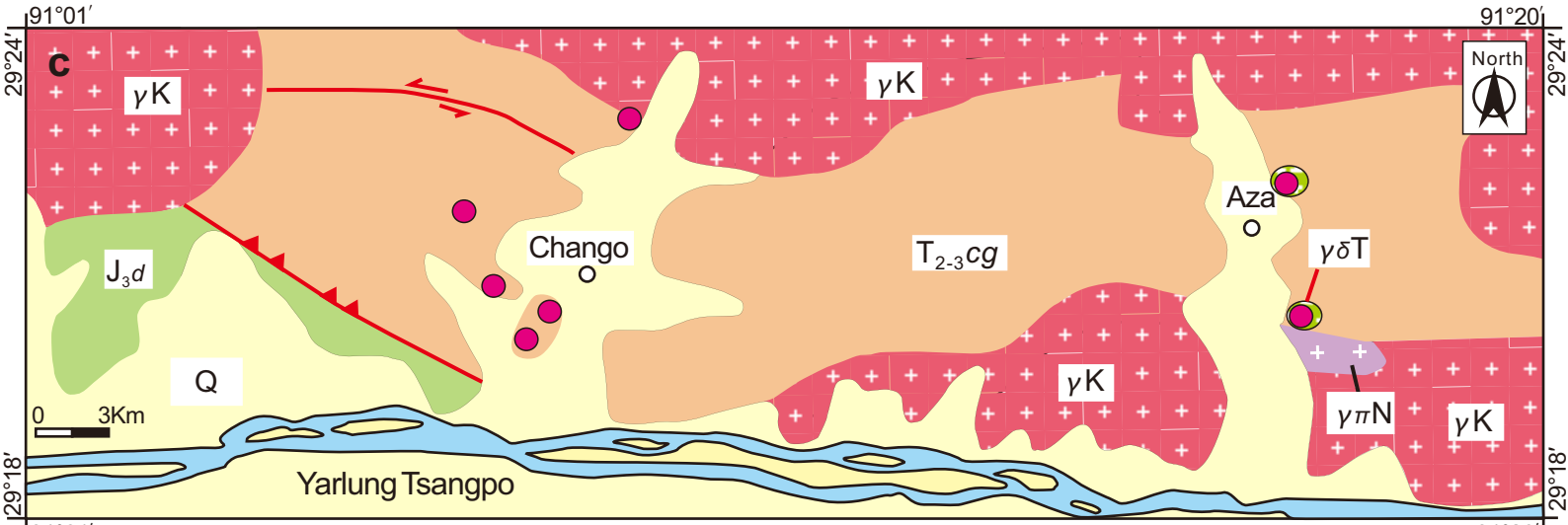

Q	Quaternary deposits	$T_{2\text{-}3}cg$	Changguo Formation		Thrust fault		Yarlung Tsangpo river
J_3d	Duodigou Formation	$\gamma\pi N$	Neogene granite porphyry		Strike-slip fault		Sample location
γK	Gangdese granite (Cretaceous)	$\gamma\delta T$	Triassic granodiorite		Town		

Figure 2

Click here to access/download;Figure;Figure 2.pdf

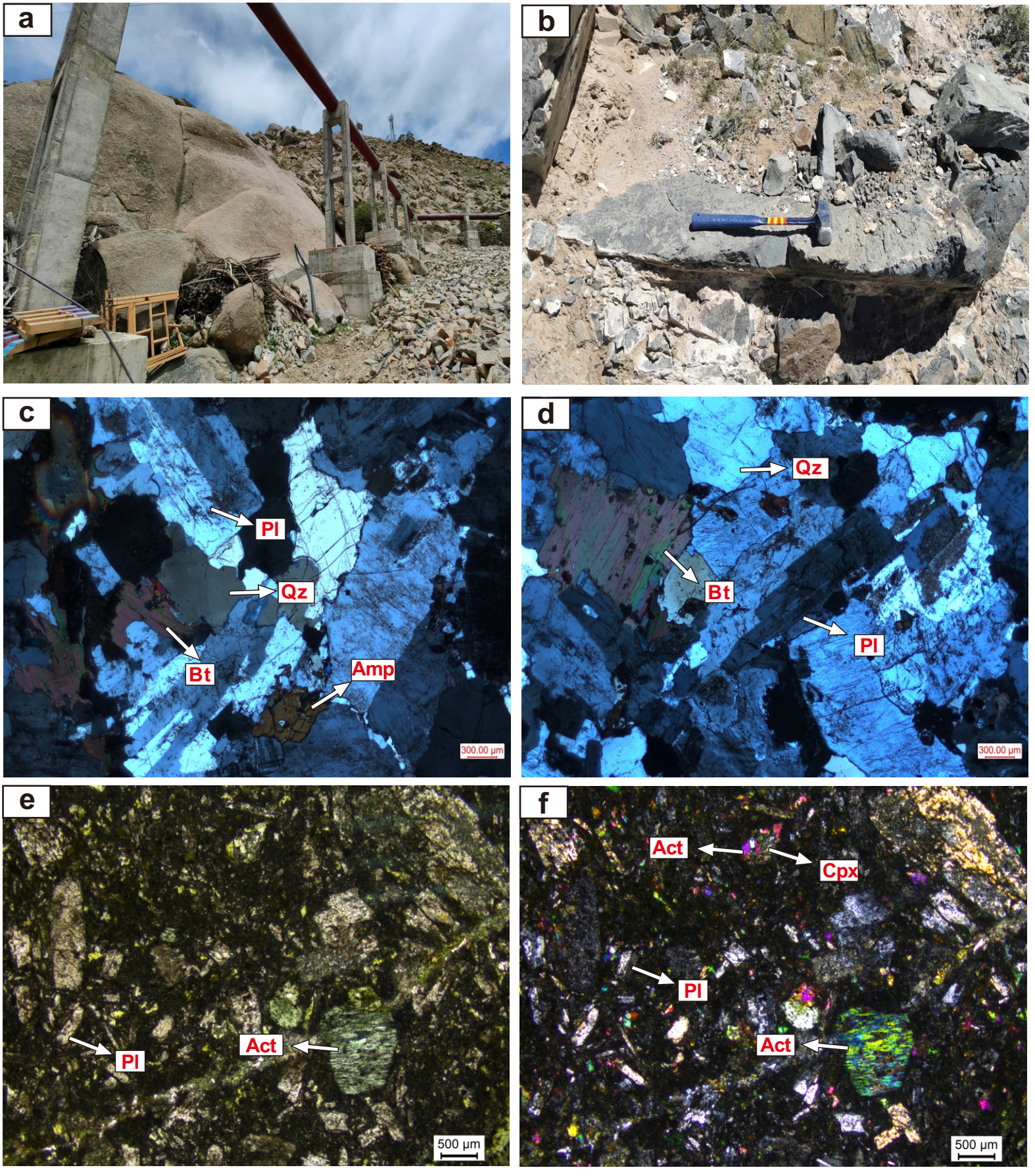

Figure 3

Click here to access/download;Figure;Figure 3.pdf

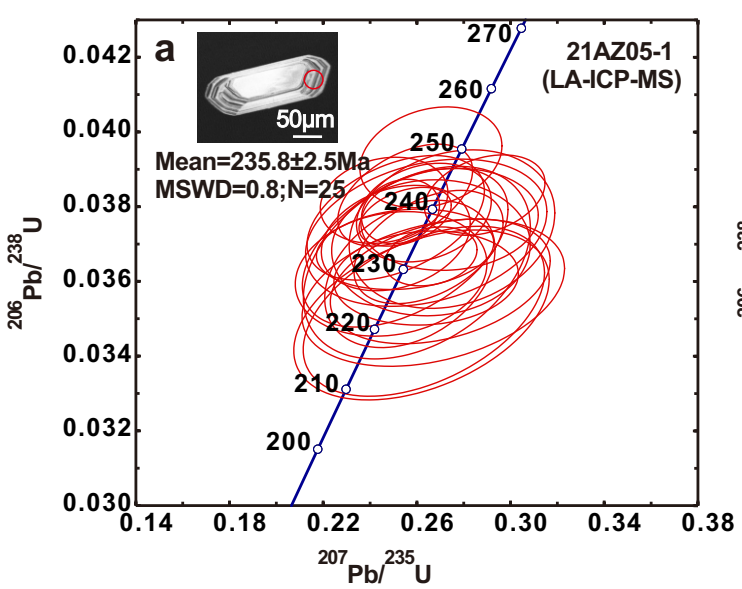

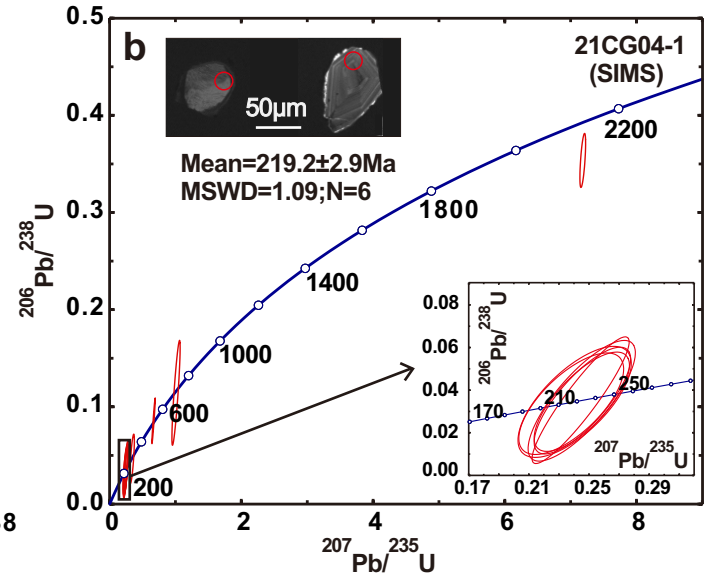

Figure 4

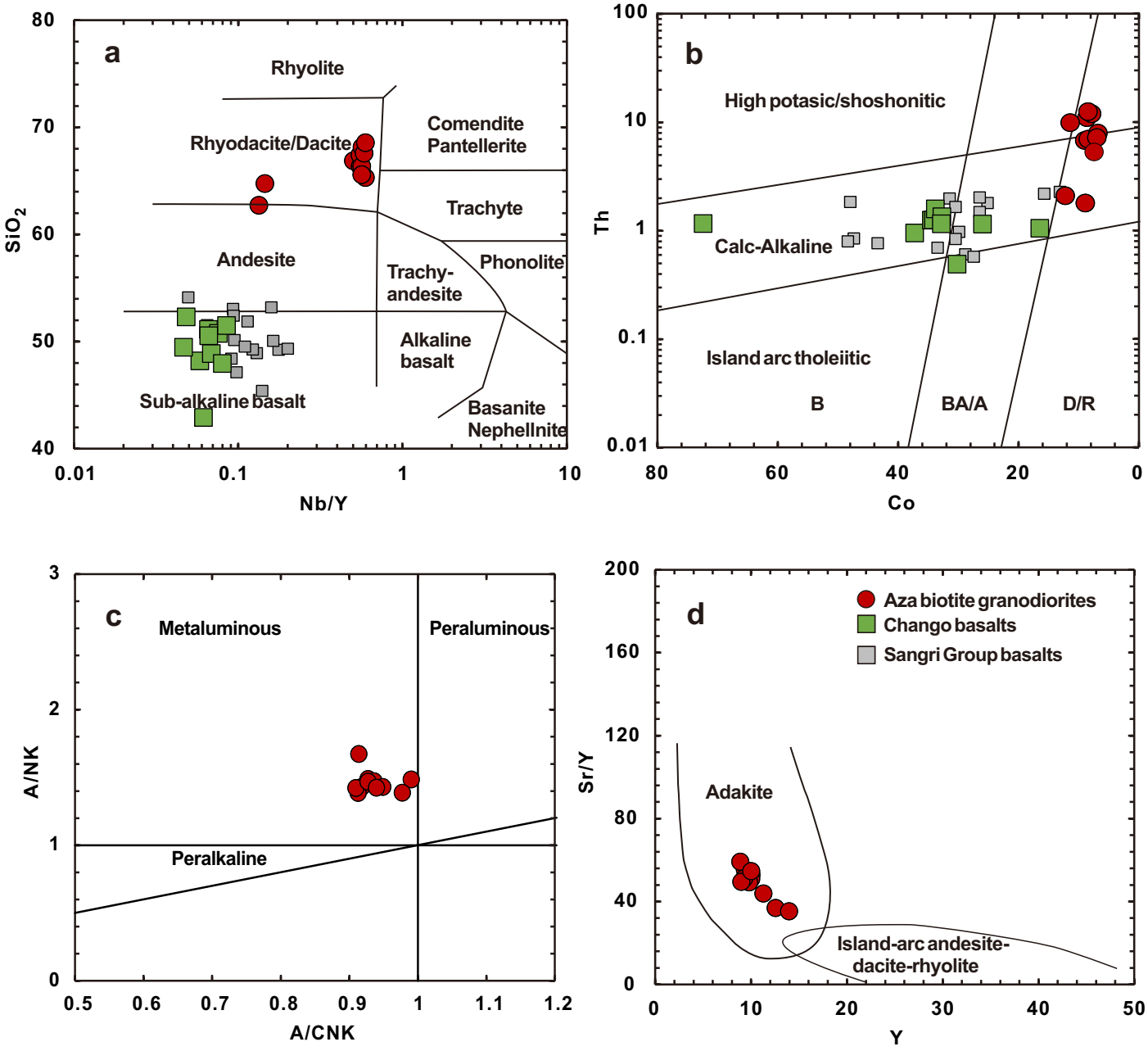

Figure 5

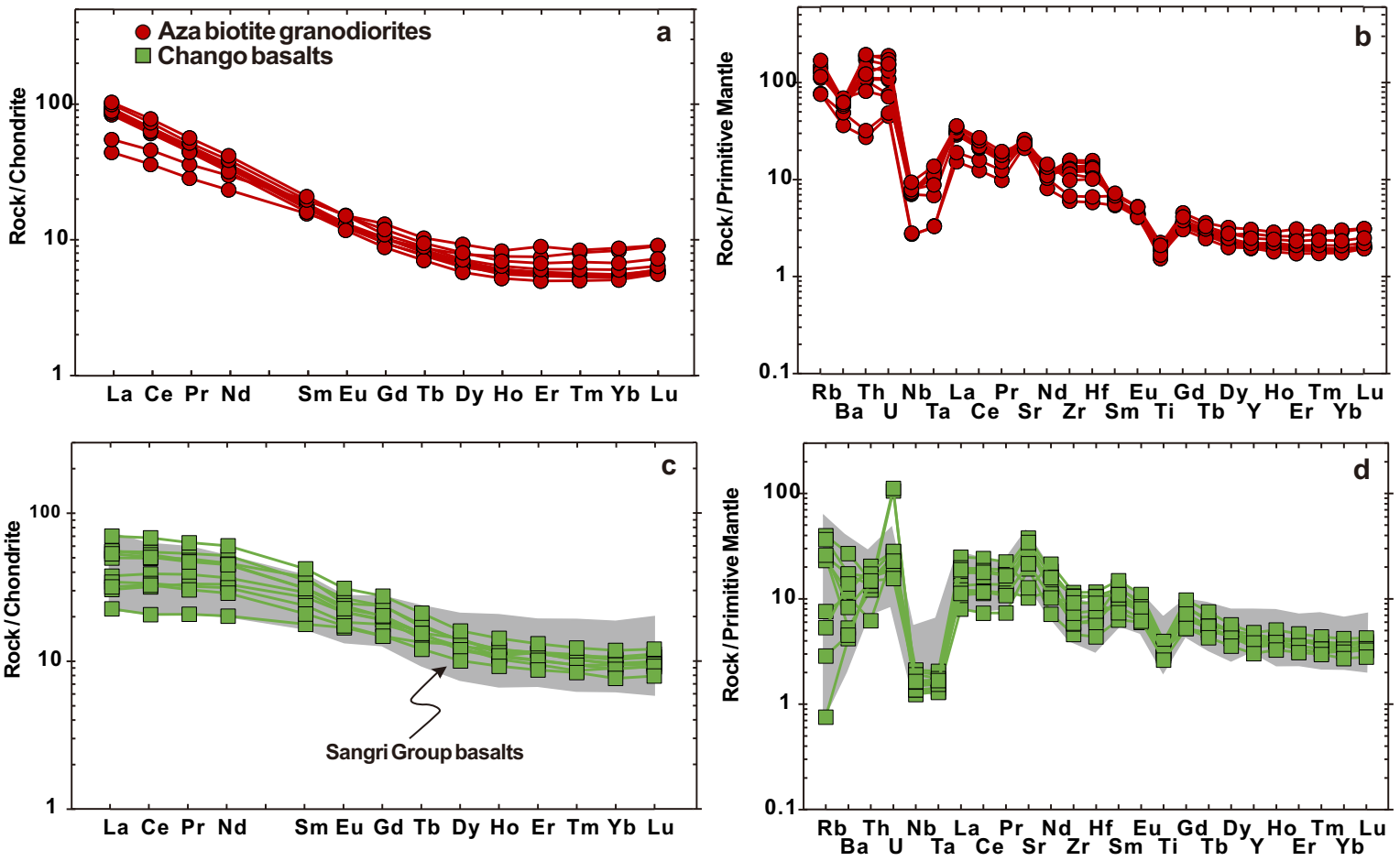

Figure 6

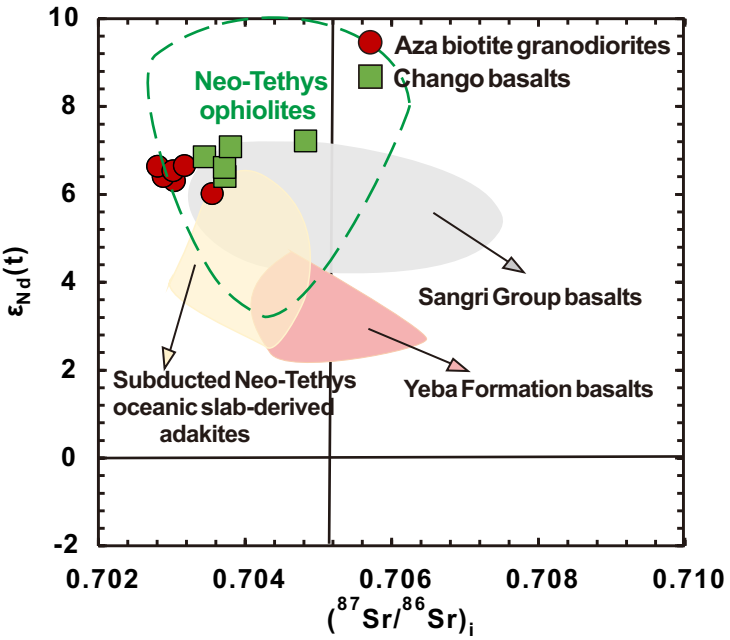

Figure 7

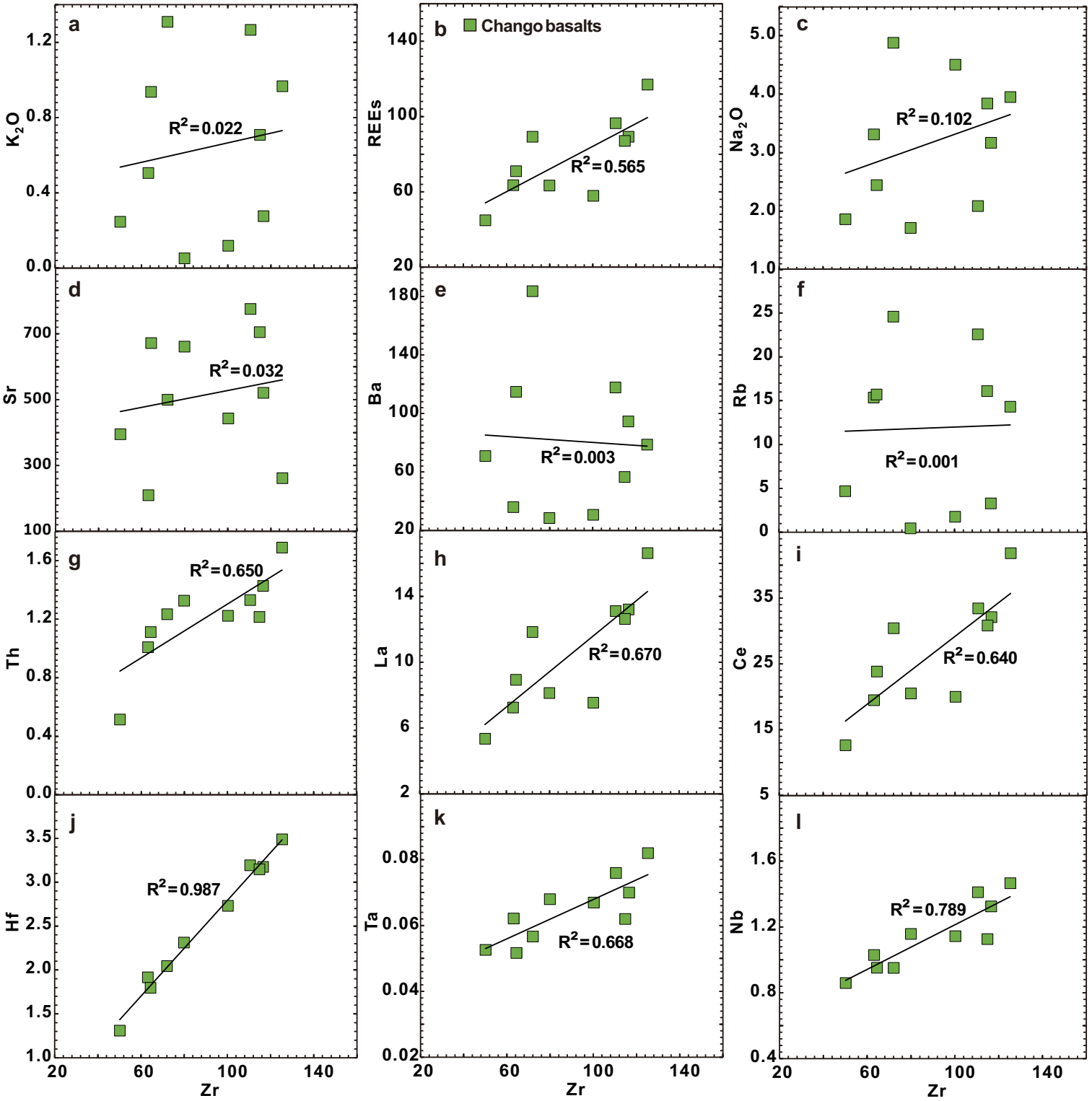

Figure 8

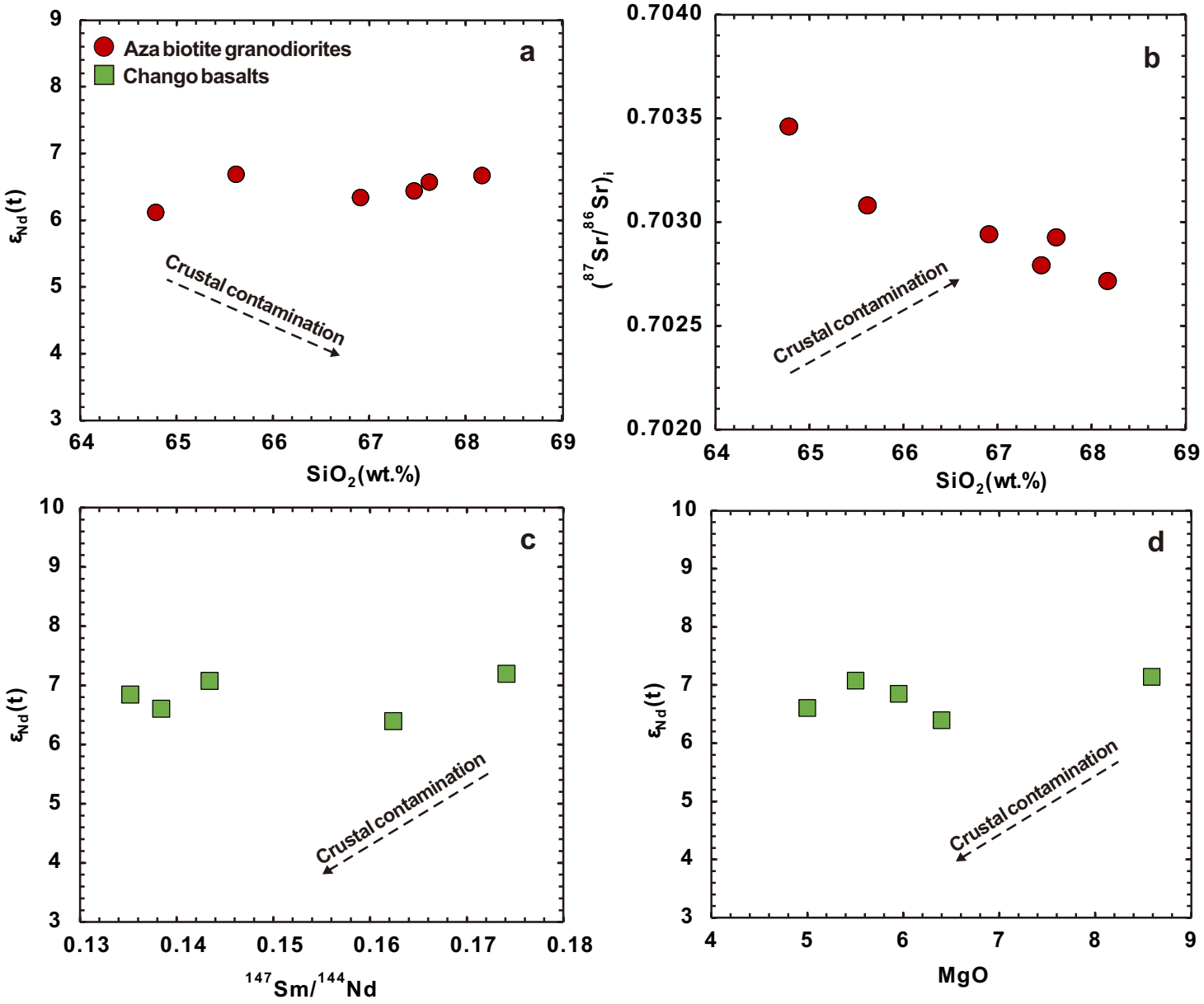

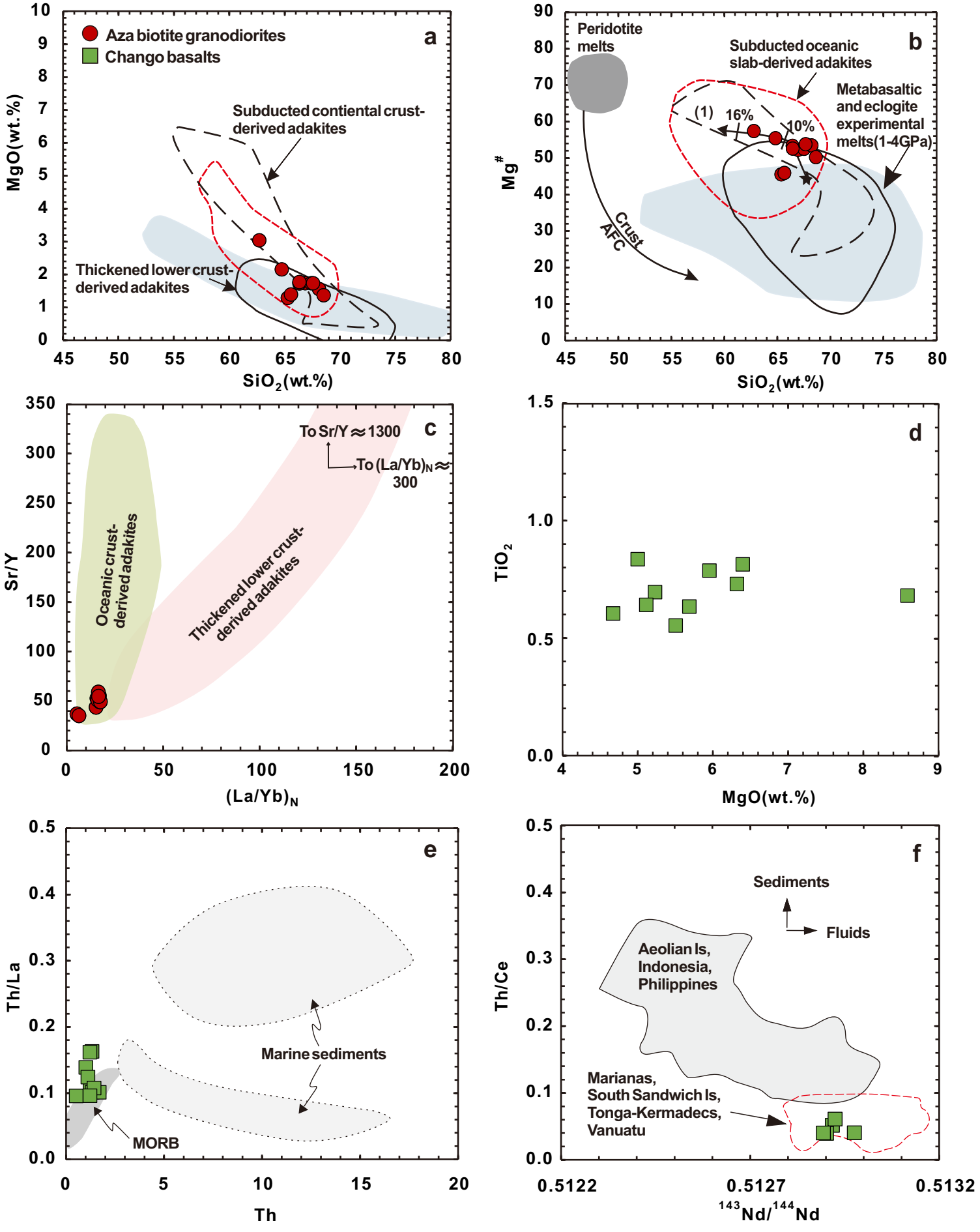

Figure 10

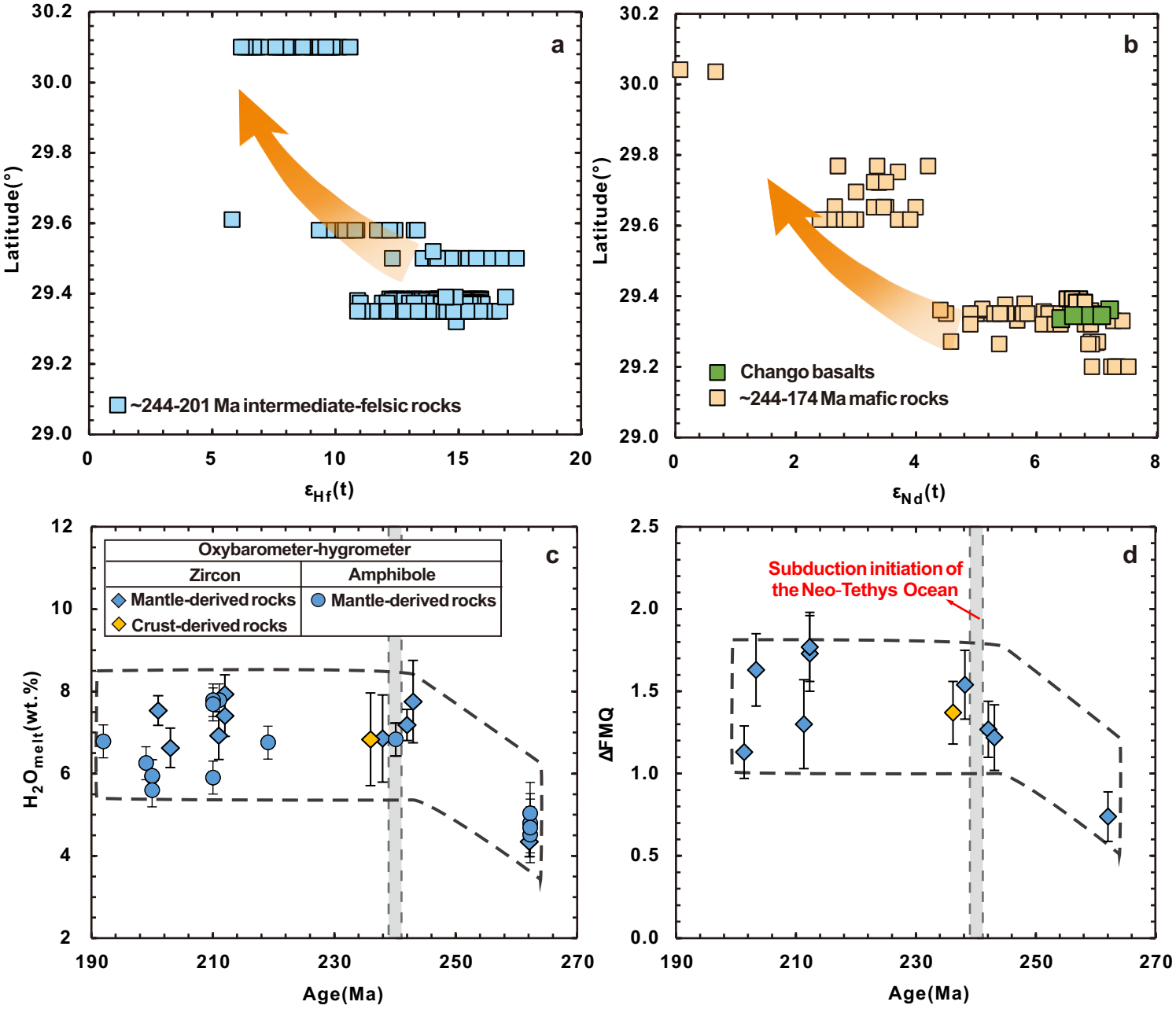

Figure 11

Click here to access/download;Figure;Figure 11.pdf

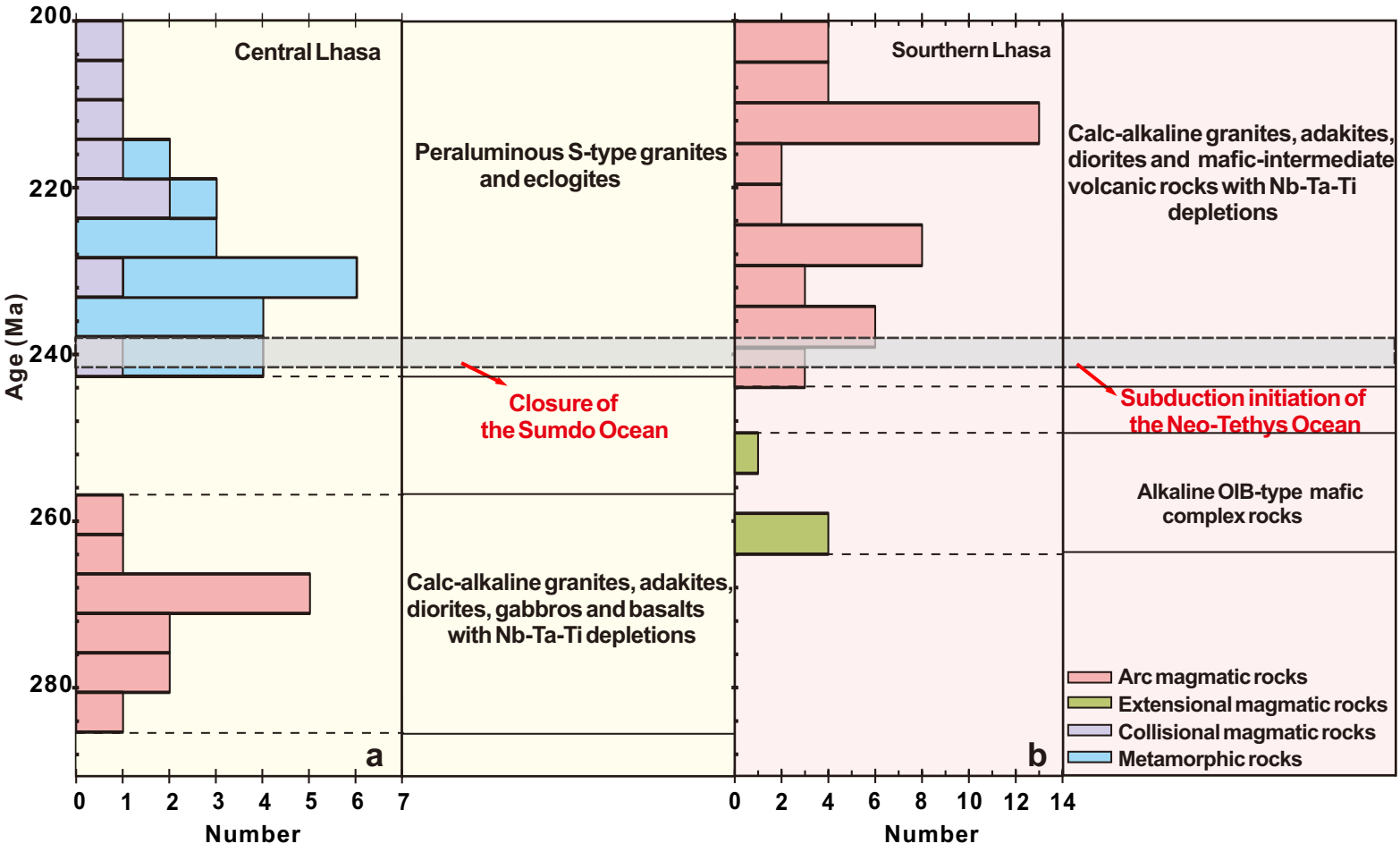

Figure 12

Click here to access/download;Figure;Figure 12.pdf

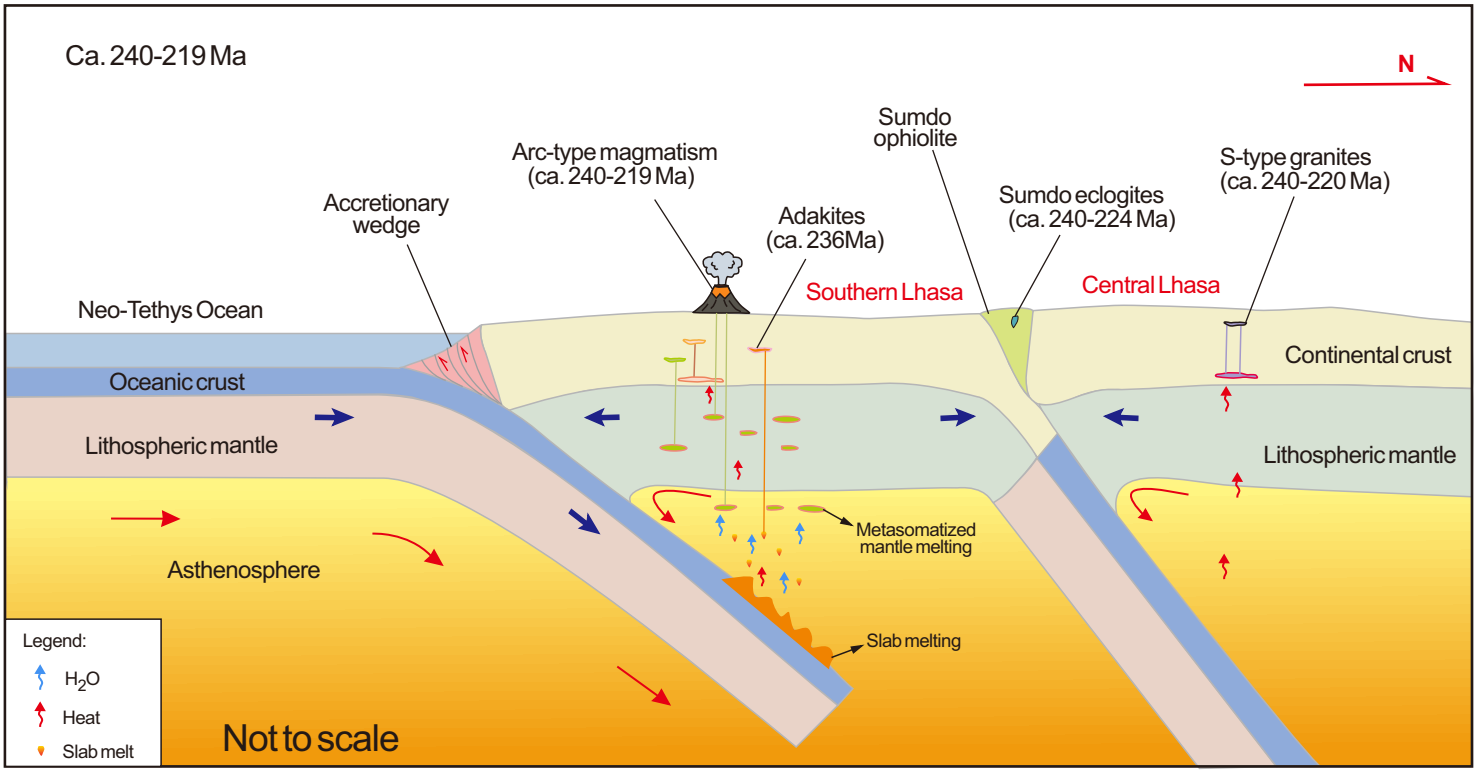

Supplementary material 1

Click here to access/download

Supplementary material/Appendix (Files for online publication only)

Supplemental material.docx

Supplementary material 2